# Unlimited Sensing for Multiband Signals:

## Theory, Algorithm and Hardware Validation

Ruiming Guo, Gal Shtendel and Ayush Bhandari

**Abstract**

Multiband signals are functions whose spectral support is confined to multiple disjoint continuous passbands. Sub-Nyquist sampling and reconstruction of such signals has long been a central topic in the signal processing community, motivated by diverse applications such as cognitive radio, radar, and communications. Despite decades of algorithmic progress, a key challenge remains: the coexistence of weak and strong components often leads to high-dynamic-range, creating an inherent trade-off between digital resolution and dynamic range in conventional acquisition systems. In line with the spirit of computational sensing, the recently proposed Unlimited Sensing Framework (USF) addresses this bottleneck by exploiting a surprising mathematical insight: smooth signals can be reconstructed entirely from their fractional part (modulo representation). While prior work has studied USF in the bandlimited setting, multiband signals still remain largely unexplored. This paper introduces a novel multiband sensing approach that achieves high-resolution reconstruction from folded, sub-Nyquist samples. The main contribution is a multiband sampling theorem, complemented by perturbation analysis and an empirically stable algorithm that operates in high-dynamic-range, bit-limited regimes. We conduct extensive numerical experiments to validate the proposed approach over a wide range of key performance metrics, such as input dynamic range, aggregate sampling rate, bit budget, etc. Narrowing the gap between theory and practice, we demonstrate the effectiveness of our method on folded hardware measurements. In crux, this work establishes a foundation for USF-enabled multiband sensing, opening new directions in theory, algorithms, and real-world applications.

**Keywords** Folding non-linearity, multiband, nonuniform periodic sampling, sub-Nyquist sampling, unlimited sampling.

This work is supported by the European Research Council's Starting Grant for "CoSI-Fold" (101166158) and UK Research and Innovation council's FLF Program "Sensing Beyond Barriers via Non-Linearities" (MRC Fellowship award no. MR/Y003926/1). Further details on Unlimited Sensing and materials on *reproducible research* are available via `https://bit.ly/USF-Link`.

The authors are with the Computational Sensing & Imaging Lab (CSIL) at the Dept. of Electrical and Electronic Engg., Imperial College London, South Kensington, London SW7 2AZ, UK. (Emails: `{ruiming.guo,g.shtendel21}@imperial.ac.uk, a.bhandari@imperial.ac.uk` or `ayush@alum.mit.edu`).

# Contents

**1 Introduction** **3**

**2 Exact Multiband Recovery via Sub-Nyquist USF** **7**

**3 Sub-Nyquist Unlimited Sensing in Practice** **16**

3.1 Sub-Problem P1: Solution Strategy . . . . . 19
3.2 Sub-Problem P2: Solution Strategy . . . . . 22

**4 Experiments** **23**

4.1 Numerical Experiments . . . . . 24
4.1.1 Near Landau Rate Recovery . . . . . 24
4.1.2 Evaluation over $B$ and $L$ . . . . . 25
4.1.3 Evaluation over $B$ and $\|g\|_{\mathbf{L}_\infty}$ . . . . . 26
4.1.4 Evaluation over Noise and $\|g\|_{\mathbf{L}_\infty}$ . . . . . 27
4.1.5 Weak-Strong Detection . . . . . 28
4.2 Folded-Hardware Proof-of-Concept . . . . . 28

**5 Conclusions** **29**

**References** **30**

## 1 Introduction

At the foundation of modern digital acquisition lies the Shannon–Nyquist theorem, which ignited the digital revolution. In his seminal work [1], Shannon established the connection between a continuous-time bandlimited signal and its discrete representation through a sequence of uniformly spaced samples. Lossless recovery is guaranteed when the sampling frequency is at least twice the maximum frequency of the signal—*the Nyquist rate*.

In practice, this sampling paradigm is realized by analog-to-digital converters (ADCs), which not only acquire uniformly spaced samples but also quantize their amplitudes onto a predefined grid. In ADC design and applications, hardware complexity and sampling cost are primarily dictated by two key metrics: (i) the sampling frequency and (ii) the quantization bit budget [2].

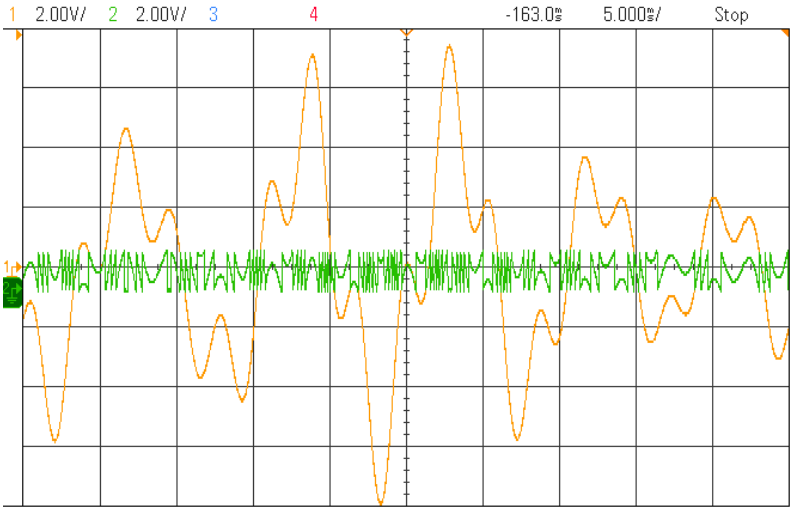


**Fig. 1.** Oscilloscope view of our USF-MC hardware prototype (see Fig. 6) output of a multiband signal comprising weak-strong mixtures within a 50ms observation window, as analyzed and recovered in Fig. 14 (see Section 4.2).

**Multiband Sampling.** In this work, we consider a sub-class of bandlimited signals whose spectrum consists of disjoint narrowbands, as illustrated in Fig. 2. Multiband signals (MBS) arise in applications such as cognitive- [18] and software-defined- radio [19]. Mathematically,

$$g(t) = \sum_{k=0}^{K_0-1} \left(\varphi_k(t)\, e^{\jmath\omega_k t} + \overline{\varphi}_k(t)\, e^{-\jmath\omega_k t}\right) \equiv \mathtt{MB}_{\Omega}^{K}(\underline{\theta}), \tag{1}$$

$$\text{where } K = 2K_0,\ \underline{\theta} = \{\varphi_k, \omega_k\}_{k\in\mathbb{I}_K},\ \varphi_k \in \mathcal{B}_{\Omega} \cap \mathbf{L}_2 \tag{2}$$

$\{\varphi_k\}_{k\in\mathbb{I}_K}$ are $\Omega$-bandlimited baseband signals and $\{\omega_k\}_{k=0}^{K-1}$ are carrier frequencies[1]. In 1967, Landau showed that the minimal sampling density required for stable recovery of a MBS in (1) is determined by the total occupied bandwidth, i.e., $K\Omega$, often referred to as the Landau rate.

Due to their wide spectral span, sampling MBS at the Nyquist rate requires high-speed ADCs. To mitigate the resulting hardware complexity and power consumption, a substantial body of work has focused on *sub-Nyquist* acquisition strategies. These approaches aim to operate near Landau's sampling bound, which is typically much lower than the Nyquist rate in the multiband setting. Pioneering works include multi-coset sampling by Bresler and co-workers [6,7,10], and

[1]Since $g(t) \in \mathbb{R}$, we can derive, for $k \in \mathbb{I}_K$, $\varphi_{K-1-k} = \overline{\varphi}_k$ and $\omega_{K-1-k} = -\omega_k$, where $\overline{(\cdot)}$ denotes the conjugate operator.

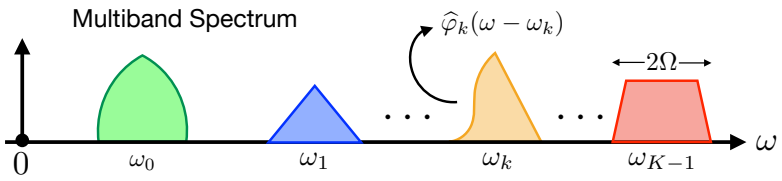


**Fig. 2.** Spectral support of a multiband signal in (1).

**Table 1.** Classification of sub-Nyquist sampling approaches under different assumptions on spectral support.

| Spectral-support assumption | Sampling approaches and representative work |
|---|---|
| **Known carriers** $\{\omega_k\}_{k=0}^{K-1}$ known | Kohlenberg studied low-rate sampling of bandpass signals ($K=2$) in [3]. *Lin & Vaidyanathan* extended periodic non-uniform sampling to MBS in [4]. These methods achieve exact recovery at rates approaching *Landau rate* [5]. |
| **Unknown carriers** $\{\omega_k\}_{k=0}^{K-1}$ unknown | Recovery with partial spectral knowledge was studied in [6–8], using multi-coset sampling without exact support but with conditions on band locations. *Herley & Wong* [9] suggested a semi-blind system, followed by works *e.g.* [10]. Using compressed sensing, *Mishali & Eldar* [11] proposed a spectrum-blind method with guaranteed reconstruction, allowing MBS recovery at arbitrary band positions. |
| **Unknown carriers, zero bandwidth** $\{\omega_k\}_{k=0}^{K-1}$ unknown, $\Omega=0$ | Here, the problem reduces to sub-Nyquist frequency estimation. Multi-channel architectures have been widely studied, including the pioneering works of *Xia et al*. [12,13] and *Vaidyanathan et al*. [14,15], as well as more recent contributions by *Fu et al*. [16,17]. |

compressed sensing–based methods by Mishali & Eldar [11,20,21]. Table 1 categorizes existing sub-Nyquist approaches based on assumptions on spectral support, and Fig. 3 places them on a timeline.

**Temporal Sampling Reduction.** In Sub-Nyquist acquisition methods, amplitude quantization imposes a severe challenge due to two main factors:

1. Lowering sampling rates reduces the number of acquired measurements, which limits reconstruction fidelity and increases sensitivity to quantization noise.

2. MBS typically exhibit a large dynamic range [22–24], imposing coarser quantization step that leads to significant quantization error.

**Amplitude-domain Bottleneck.** Taken together, these factors necessitate a high ADC bit budget to accommodate DR and ensure digital resolution. Indeed, practical realisations of existing approaches rely on high-resolution ADCs. For example, Xampling systems employ $\sim$ 16-bit quantization [25], Random Demodulator prototypes deploy $\sim$ 12 bits [26], and multi-coset realizations use $\sim$ 14 bits [27]. Since the ADC power consumption scales approximately exponentially with the number of bits, using high-resolution ADCs may offset the hardware and power savings achieved by sub-Nyquist sampling. This amplitude DR-quantization issue is largely overlooked in the existing literature.

**The Unlimited Sensing Framework (USF).** The USF, introduced in [28–30], is a sampling paradigm that overcomes the fundamental trade-off between high-dynamic-range (HDR) and

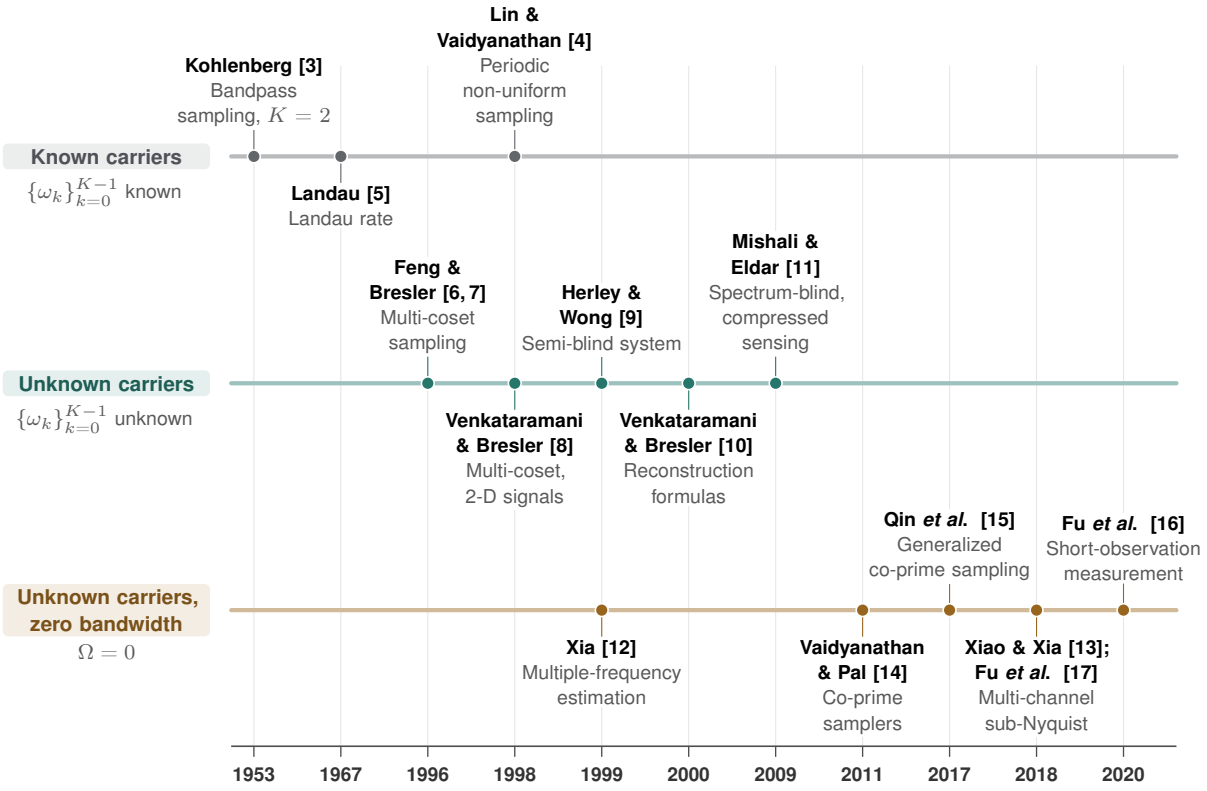


**Fig. 3.** Timeline of the sub-Nyquist sampling works summarised in Table 1, grouped by spectral-support assumption. Years are evenly spaced (not to scale).

high-digital-resolution (HDRes). In the USF, samples of a signal $g$ are acquired using modulo ADCs [30–33], which first encode the input into a folded signal $\mathscr{M}_\lambda(g)$ according to

$$\mathscr{M}_\lambda : g \mapsto 2\lambda \left( \left[\!\!\left[ \frac{g}{2\lambda} + \frac{1}{2} \right]\!\!\right] - \frac{1}{2} \right), \quad [\![g]\!] \stackrel{\text{def}}{=} g - \lfloor g \rfloor, \quad \lambda > 0, \tag{3}$$

where $\lfloor g \rfloor = \sup\{k \in \mathbb{Z} \mid k \leqslant g\}$ denotes the integer part of $g$, and subsequently quantize it. By construction, $|\mathscr{M}_\lambda(g)| \leqslant \lambda$, so quantization is performed over the fixed interval $[-\lambda, \lambda)$, independent of the dynamic range of $g$, improving the digital resolution for a given bit budget.

The modulo hardware mapping (3) is non-linear and many-to-one, making recovery of $g$ an inverse problem that requires dedicated reconstruction algorithms, including single-channel methods [28, 34–38] and multi-channel approaches [39, 40]. From a theoretical standpoint, reconstruction guarantees from folded measurements have been studied over a wide range of signal classes, such as bandlimited signals [29, 41–43], sparse vectors [44, 45], shift-invariant signals [46], and sparse signals [47].

**Motivation, Challenges and Related Work.** The USF provides a principled approach to addressing the amplitude quantization bottleneck in sampling, enabling HDRes even with low-resolution ADCs. As such, it offers a promising direction for sub-Nyquist acquisition, mitigating the reliance on high bit budgets in existing architectures.

Nevertheless, recovering multiband signals from folded samples at sub-Nyquist rates—referred to here as sNyq$\lambda$-MB —introduces unique algorithmic challenges. In particular, operating below the Nyquist rate reduces measurement redundancy, whereas existing

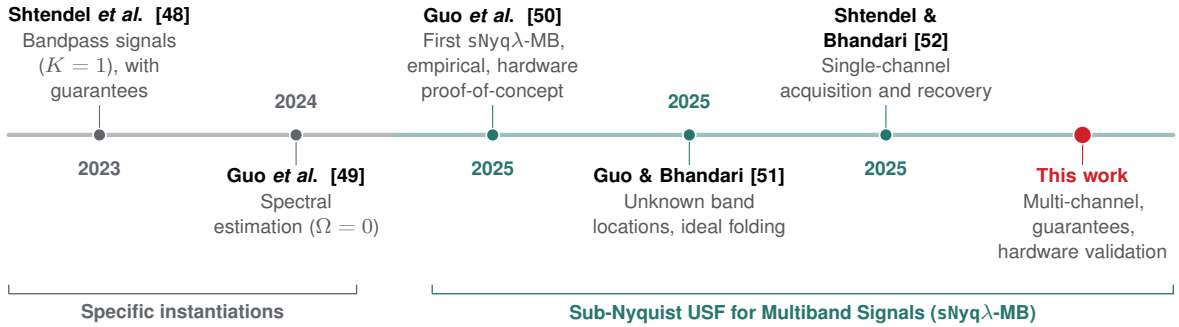


**Fig. 4.** Timeline of the USF-based sub-Nyquist works discussed above, from specific instantiations of sNyq$\lambda$-MB to the present multi-channel approach. Milestones are evenly spaced (not to scale).

USF approaches rely on oversampling to enable reliable signal reconstruction. More specifically, the sNyq$\lambda$-MB setting raises the following questions:

- Q1 What is the sampling criterion?
- Q2 How to design a stable recovery approach?
- Q3 What are the operational limits of the recovery algorithm in practice?

These questions remain open as this topic is still in its nascent stages.

Previously, specific instantiations of sNyq$\lambda$-MB have been investigated (see Fig. 4). For bandpass signals ($K = 1$ in (1)), a below-Nyquist method with theoretical guarantees was reported in [48]. Sub-Nyquist spectral estimation ($\Omega = 0$ in (1)) was studied in [49], achieving 1200-fold downsampling and 33-fold resolution enhancement. The first attempt at sNyq$\lambda$-MB appeared in [50], presenting an empirical algorithm with proof-of-concept hardware validation but without theoretical guarantees or resilience to hardware-induced non-idealities. A subsequent study [51] addressed sNyq$\lambda$-MB with *unknown band locations* under the assumptions of ideal folding and a single baseband model ($\varphi_k = \varphi_{k'}, \{k, k'\} \in \mathbb{I}_K$), providing theoretical guarantees with no hardware validation.

The recent work [52] studied the signal model in (1) and proposed a recovery method under a single-channel architecture, utilizing additional spectral separation assumptions. The present work adopts a multi-channel acquisition design, offering recovery guarantees, enhanced algorithmic capabilities, and a broader scope of experimental validation.

**Contributions.** This paper addresses the above questions: Q1 to Q3. Distinct from prior USF works that require temporal oversampling, the core contribution lies in the multi-channel modulo sampling theorem for generic multiband signals, complemented by perturbation analysis together with numerical and hardware-in-the-loop validation.

1. **Theory.** We develop sampling criterion of recovering generic multiband signals from sub-Nyquist folded samples. We provide aggregate-rate comparison relative to the Landau rate and performance analysis under perturbation/timing jitter.
2. **Algorithm.** We develop an empirically stable algorithm (sNyq$\lambda$-PMB) that can handle *measurement distortions and hardware non-idealities*. Establishing on the non-convex optimization scheme, our algorithm accurately recovers the MBS by performing sparse approximation across channels.
3. **Experimental Validation.** We conduct extensive numerical experiments to verify the derived

theoretical results and recovery method. Bridging the gap between theory and practice, we perform hardware-in-the-loop validation, showcasing precise signal recovery with mean-squared error (MSE) down to $-31.33$ dB, using low-resolution acquisition.

**Notation.** Let $\mathbb{Z}, \mathbb{R}$ and $\mathbb{C}$ denote integers, real and complex numbers, respectively. We use $\mathbb{I}_N = \{0, \cdots, N-1\}, N \in \mathbb{Z}^+$ to denote the set of $N$ contiguous integers. Continuous functions and discrete sequences are written as $g(t), t \in \mathbb{R}$ and $g[n]$, respectively. Vectors and matrices are written in bold lowercase and uppercase fonts, *e.g.* $\mathbf{g} = [g[0] \ \cdots \ g[N-1]]^\top \in \mathbb{R}^N$ and $\mathbf{G} = [g_{n,m}]_{n\in\mathbb{I}_N}^{m\in\mathbb{I}_M} \in \mathbb{R}^{N\times M}$. The column submatrix of $\mathbf{G} \in \mathbb{R}^{N\times M}$ is denoted as $\mathbf{G}(\mathcal{S})$ where $\mathcal{S} \subseteq \mathbb{I}_M$ is the selected column index set. The $\mathbf{L}_p(\mathbb{R})$ space equipped with the $p$-norm is the standard Lebesgue space; $\mathbf{L}_\infty$ denotes the space of bounded functions. Spaces associated with sequences are written as $\ell_p$. The max-norm ($\mathbf{L}_\infty$) of a function is defined as $\|g\|_{\mathbf{L}_\infty} = \inf\{c_0 \geqslant 0 : |g(t)| \leqslant c_0\}$; for sequences, $\|g\|_{\ell_\infty} = \max_n |g[n]|$. The $\mathbf{L}_2$-norm of a function is $\|g\|_{\mathbf{L}_2} = \left(\int |g(t)|^2 dt\right)^{1/2}$, while for sequences $\|g\|_{\ell_2} = \left(\sum_{n=0}^{N-1} |g[n]|^2\right)^{1/2}$.

The vector space of polynomials with complex coefficients and degrees no greater than $K$ is denoted by $P_K$; for instance, $\mathsf{Q}(z) = \sum_{k=0}^{K} h_k z^k \in P_K$. Function derivative is denoted by $\partial_t g(t)$, while for sequences the finite difference is $(\Delta g)[n] = g[n+1] - g[n]$. The Fourier Transform of $g \in \mathbf{L}_1$ is defined by $\widehat{g}(\omega) = \int_{\mathbb{R}} g(t) e^{-\jmath\omega t} dt$. The Discrete Fourier Transform (DFT) of a sequence $\mathbf{g} \in \ell^1$ is denoted by $\widehat{g}[m] = \sum_{n=0}^{N-1} g[n] e^{-\jmath\frac{2\pi mn}{N}}$.

Let $\mathbf{V}_N^M$ denote the $N \times M$ Vandermonde matrix $\mathbf{V}_N^M = \left[\xi_N^{n\cdot m}\right]_{n\in\mathbb{I}_N}^{m\in\mathbb{I}_M}$, where $\xi_N^n = e^{\jmath\frac{2\pi n}{N}}$. Diagonal matrices are denoted by $\mathscr{D}_K(\mathbf{h})$ with $[\mathscr{D}_K(\mathbf{h})]_{k,k} = [\mathbf{h}]_{k\in\mathbb{I}_K}$. We use $(f \circ g)(t) = f(g(t))$ to denote function composition. Define the shift-difference operator $\mathcal{S}_{T_d}$ as $\mathcal{S}_{T_d}(\cdot) = (\cdot)(t + T_d) - (\cdot)(t)$. The mean-squared error (MSE) between $\mathbf{x}, \mathbf{y} \in \mathbb{R}^N$ is defined as

$$\mathcal{E}_2(\mathbf{x}, \mathbf{y}) \stackrel{\text{def}}{=} \frac{1}{N} \sum_{n=0}^{N-1} |x[n] - y[n]|^2 . \tag{4}$$

## 2 Exact Multiband Recovery via Sub-Nyquist USF

**Multi-Channel USF Sampling Architecture.** Here, we focus on the MBS reconstruction with known band locations. On the one hand, recovery from modulo non-linearity requires oversampling, *i.e.* super-Nyquist sampling. On the other hand, the multiband structure naturally calls for sub-Nyquist sampling. To resolve this stalemate, we propose a multi-channel USF sampling pipeline (`USF-MC`), as shown in Fig. 5. By design, the input HDR signal $g(t)$ is first folded in analog-domain, yielding a continuous-time, low-dynamic-range (LDR) signal, $y(t) = \mathscr{M}_\lambda(g(t))$. Subsequently, $y(t)$ is sampled pointwise through multiple channels with time-delays, yielding,

$$y_n^l = y(t)|_{t=nT+lT_d}, \ \ n \in \mathbb{I}_N, \ \ l \in \mathbb{I}_L. \tag{5}$$

In real-world scenarios, since the modulo-folding occurs in analog-domain, noise arises from (i) thermal noise that follows a Gaussian distribution [53] and (ii) quantization noise that follows a uniform distribution. Thus, the noisy, "distorted" `USF-MC` measurements can be modelled as [49],

$$y_{n,w}^l = y_n^l + w_n^l \tag{6}$$

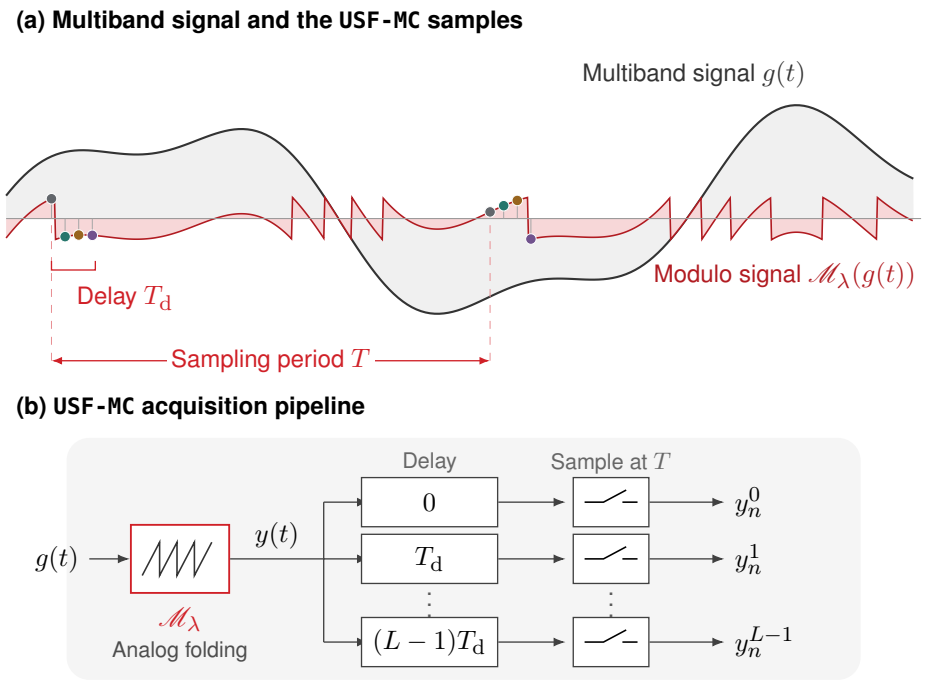


**Fig. 5.** Multi-channel USF sampling architecture (USF-MC). The input HDR signal $g(t)$ is firstly being folded in analog-domain (see Fig. 1), yielding the LDR signal $y(t)$ as shown in (a). Subsequently, the folded signal $y(t)$ is sampled pointwise through multiple channels with time-delays.

where $w$ represents the measurement noise and folding non-idealities [30]. In the next sections, our goal is to 1) investigate the sampling criterion for perfect recovery in the noiseless case, 2) develop empirically stable recovery method that can tolerate measurement noise and distortion, and 3) validate the algorithm performance through experiments.

**Exact Multiband Signal Recovery.** To capture at sub-Nyquist rates, we assume

$$T > \frac{\pi}{\Omega_K + \Omega}, \ \Omega_K = \max_k |\omega_k| \,. \tag{7}$$

Recovering $g(t)$ from $\{y_n^l\}_{n\in\mathbb{I}_N}^{l\in\mathbb{I}_L}$ thus requires inverting two non-linear foldings: (i) amplitude folding when $|g(t)| > \lambda$, and (ii) spectral folding due to aliasing from sub-Nyquist sampling. In this regime, existing USF unfolding methods [29,30,54] fail, as they rely on oversampling-induced sample correlation.

To address this problem, we adopt a *divide-and-conquer* strategy. First, we decouple the modulo folding $\mathscr{M}_\lambda(\cdot)$ through non-linear amplitude filtering, trading *channel redundancy* for *temporal redundancy* to recover $g_n^l$ from $y_n^l$ alone. Next, we reconstruct the MBS directly in the higher-order differences (HoD) domain, thereby avoiding explicit modulo inversion. This approach enables recovery with theoretical guarantees, as stated in the theorem below.

**Theorem 1.** *Let $g(t) = \mathtt{MB}_{\Omega}^{K}(\underline{\theta})$ and the* `USF-MC` *samples be $y_n^l = \mathscr{M}_\lambda(g(nT + lT_d))$, $n \in \mathbb{Z}, l \in \mathbb{I}_L$ with $T = PT_d$, $P \in \mathbb{Z}^+$ and known $\{\omega_k\}_{k=0}^{K-1}$. Then, $g(t)$ can be perfectly reconstructed if*

$$T_d < \frac{1}{\Omega_K + \Omega}, \qquad P \in \left(\frac{\pi}{(\min_k |\omega_k| - \Omega)T_d}, \frac{\pi}{\Omega T_d}\right], \qquad L \geqslant h + K, \tag{8}$$

*and $\mathbf{B}$ has a full Kruskal-rank[a], where*

$$[\mathbf{B}]_{l,p} = e^{\jmath \frac{2lp\pi}{P}}, \quad l \in \mathbb{I}_{L-h}, \quad |p| = 1, \cdots, \left\lfloor \frac{P}{2} \right\rfloor, \qquad h = \left\lceil \frac{\ln \lambda - \ln \|g\|_{\mathbf{L}_\infty}}{\ln((\Omega + \Omega_K) T_d)} \right\rceil. \tag{9}$$

[a] The *Kruskal-rank* of a matrix $\mathbf{A}_h$ is the maximal number $L$ such that every set of $L$ columns of $\mathbf{A}_h$ is linearly independent [55].

*Proof.* We first show amplitude shrinkage along channel dimension by deriving the sampling criteria and then deliver the direct MBS reconstruction in the modulo domain.

**Amplitude Shrinkage Across Channels.** Let us define $g_n^l = g(nT + lT_d)$ and $y_n^l = y(nT + lT_d)$, respectively. We use $\{\Delta^{(h)} g_n^l, \Delta^{(h)} y_n^l\}$ to represent the $h$-th order difference of $\{g_n^l, y_n^l\}_{l=0}^{L-1}$ ($n$ is fixed). With $\mathcal{S}_{T_d}$, we can derive that,

$$\Delta^{(h)} g_n^l = \mathcal{S}_{T_d}^{(h)}(g)(t)\Big|_{t=nT+lT_d}, \quad \mathcal{S}_{T_d}^{(h)} = \mathcal{S}_{T_d} \circ \mathcal{S}_{T_d}^{(h-1)}. \tag{10}$$

Next, we show that the following property holds,

$$\forall g \in \mathtt{MB}_{\Omega}^{K}(\cdot) \implies \left\|\mathcal{S}_{T_d}\right\|_{\mathbf{L}_\infty} \leqslant \beta \stackrel{\text{def}}{=} (\Omega + \Omega_K) T_d. \tag{11}$$

By definition, we can compute,

$$\left\|\mathcal{S}_{T_d}(g)\right\|_{\mathbf{L}_\infty} \leqslant \|\partial_t g\|_{\mathbf{L}_\infty} T_d \leqslant (\Omega_K + \Omega)\left(T_d \|g\|_{\mathbf{L}_\infty}\right) \tag{12}$$

which follows Bernstein's inequality since $g \in \mathcal{B}_{\Omega_K + \Omega}$ [56]. Hence, we derive, $T_d < \frac{1}{\Omega_K + \Omega} \implies \left\|\mathcal{S}_{T_d}\right\|_{\mathbf{L}_\infty} < 1$. By induction, we have,

$$\|\mathcal{S}_{T_d}^{(h)}(g)\|_{\mathbf{L}_\infty} \leqslant \beta \|\mathcal{S}_{T_d}^{(h-1)}(g)\|_{\mathbf{L}_\infty} \leqslant \cdots \leqslant \beta^h \|g\|_{\mathbf{L}_\infty}. \tag{13}$$

Since $\|\Delta^{(h)} g_n^l\|_{\ell_\infty} \leqslant \|\mathcal{S}_{T_d}^{(h)}(g)\|_{\mathbf{L}_\infty}$, we then obtain that,

$$h \geqslant \left\lceil \frac{\ln \lambda - \ln \|g\|_{\mathbf{L}_\infty}}{\ln \beta} \right\rceil \implies \left\|\Delta^{(h)} g_n^l\right\|_{\ell_\infty} \leqslant \lambda \tag{14}$$

which leads to $\mathscr{M}_\lambda(\Delta^{(h)} g_n^l) = \Delta^{(h)} g_n^l$. To access $\Delta^{(h)} g_n^l$ from $\Delta^{(h)} y_n^l$, we start with the modular decomposition [29],

$$g = \mathscr{M}_\lambda(g) + \varepsilon_g, \quad \varepsilon_g(t) = \sum_{m=0}^{M-1} c_m u(t - \tau_m) \tag{15}$$

where $u(\cdot)$ represents the unit step function, $c_m \in 2\lambda\mathbb{Z}$ and $\tau_m \in \mathbb{R}$ denote the folding amplitude

and instant, respectively. Hence, with (15), $\Delta^{(h)} g_n^l$ can be decomposed as,

$$\Delta^{(h)} g_n^l = \Delta^{(h)} y_n^l + \Delta^{(h)} \varepsilon_{g,n}^l, \;\; \Delta^{(1)} g_n^l = g_n^{l+1} - g_n^l \tag{16}$$

leading to the retrieval of $\Delta^{(h)} g_n^l$ via non-linear filtering,

$$\mathscr{M}_\lambda(\Delta^{(h)} y_n^l) = \mathscr{M}_\lambda(\Delta^{(h)} g_n^l) \overset{(14)}{=} \Delta^{(h)} g_n^l. \tag{17}$$

**Multiband Signal Recovery.** In the second part, we show direct signal recovery in HoD domain, avoiding the ambiguity caused by anti-difference operations as existing multiband sensing approaches deal with $g_n^l$.

Our starting point is the Poisson summation formula [57],

$$\sum_{n\in\mathbb{Z}} \frac{g\left(nPT_d + lT_d\right)}{e^{\jmath\omega(nPT_d+lT_d)}} = \sum_{p\in\mathbb{Z}} \frac{e^{\jmath\frac{2lp\pi}{P}}}{PT_d} \widehat{g}\left(\omega + \frac{2p\pi}{PT_d}\right) \tag{18}$$

where $\widehat{g}\left(\omega\right) = \int_{\mathbb{R}} g\left(t\right) e^{-\jmath\omega t} dt$ and $T = PT_d, P \in \mathbb{Z}^+$. Since $g \in \mathcal{B}_{\Omega_K+\Omega}$ and $T_d < \frac{1}{\Omega_K+\Omega}$, then (18) reduces to,

$$\sum_{n\in\mathbb{Z}} \frac{g\left(nPT_d + lT_d\right)}{e^{\jmath\omega(nPT_d+lT_d)}} = \sum_{p=-P_0}^{P_0} \frac{e^{\jmath\frac{2lp\pi}{P}}}{PT_d} \widehat{g}\left(\omega + \frac{2p\pi}{PT_d}\right) \tag{19}$$

where $P_0 = \lfloor P/2 \rfloor$[2]. Within the bandlimited region of interest, *i.e.* $\omega \in [-\frac{\pi}{T_d}, \frac{\pi}{T_d}]$, plugging $\mathcal{S}_{T_d}$ into equation above leads to,

$$\sum_{n\in\mathbb{Z}} \frac{\mathcal{S}_{T_d}\left(g\right)\left(t_n^l\right)}{e^{\jmath\omega(nPT_d+lT_d)}} = \sum_{p=-P_0}^{+P_0} \frac{e^{\jmath\frac{2lp\pi}{P}}(e^{\jmath(\omega T_d+\frac{2p\pi}{P})}-1)\widehat{g}\left(\omega + \frac{2p\pi}{PT_d}\right)}{PT_d} \tag{20}$$

where $t_n^l = nT + lT_d$. This can be interpreted as the low-pass filtering induced by $\mathcal{S}_{T_d}$. By induction, we can write,

$$\sum_{n\in\mathbb{Z}} \frac{\mathcal{S}_{T_d}^{(h)}(g)(t_n^l)}{e^{\jmath\omega(nPT_d+lT_d)}} = \sum_{p=-P_0}^{P_0} \frac{e^{\jmath\frac{2lp\pi}{P}}(e^{\jmath(\omega T_d+\frac{2p\pi}{P})}-1)^h\widehat{g}\left(\omega + \frac{2p\pi}{PT_d}\right)}{PT_d}. \tag{21}$$

Given the hypothesis on $P$ and $\{\omega_k\}$, we can obtain that,

$$\min_k |\omega_k| - \Omega > \frac{\pi}{PT_d} \geqslant \Omega. \tag{22}$$

[2]Without loss of generality, we assume $P$ is odd.

Hence, (22) suggests, $\widehat{g}(\omega) = 0$, $\forall \omega \in [-\frac{\pi}{PT_d}, \frac{\pi}{PT_d}]$. From (10) and (22), for every $\omega \in [-\frac{\pi}{PT_d}, \frac{\pi}{PT_d}]$, (21) translates to,

$$\sum_{|p|=1}^{P_0} \frac{[\mathbf{A}_h]_{l,p}}{PT_d} \widehat{g}\left(\omega + \frac{2p\pi}{PT_d}\right) \overset{(10)}{=} \sum_{n\in\mathbb{Z}} \frac{\Delta^{(h)} g_n^l}{e^{\jmath\omega(nPT_d + lT_d)}}. \tag{23}$$

The entries of $\mathbf{A}_h \in \mathbb{C}^{(L-h)\times(P-1)}$ are

$$[\mathbf{A}_h]_{l,p} = e^{\jmath\frac{2lp\pi}{P}} \left(e^{\jmath\left(\omega T_d + \frac{2p\pi}{P}\right)} - 1\right)^h. \tag{24}$$

Note that (23) gives rise to a system of linear equations with at most $K$ non-zero unknowns ($P \leqslant \pi/(\Omega T_d)$ in (22)). In the above, $\mathbf{A}_h(\mathcal{S}_\omega)$ can be decomposed as,

$$\mathbf{A}_h(\mathcal{S}_\omega) = \mathbf{B}\mathbf{C}_h(\mathcal{S}_\omega). \tag{25}$$

Here, $[\mathbf{B}]_{l,p} = e^{\jmath\frac{2lp\pi}{P}}$ and $\mathbf{C}_h(\mathcal{S}_\omega) = \mathscr{D}_K(\mathbf{c}_h)$. The set $\mathcal{S}_\omega$ represents the active column index set available from known carrier locations, satisfying $|\mathcal{S}_\omega| \leqslant K$ and

$$[\mathbf{c}_h]_p = (e^{\jmath(\omega T_d + \frac{2p\pi}{P})} - 1)^h, p \in \mathcal{S}_\omega. \tag{26}$$

By assumption, we can deduce that, $\mathbf{A}_h(\mathcal{S}_\omega)$ has a full Kruskal-rank as well as $\mathbf{B}$. Hence, $\{\widehat{g}\left(\omega + \frac{2p\pi}{PT_d}\right)\}_{p=-P_0}^{P_0}$ can be reconstructed exactly by solving (23), resulting in the recovery of $g$. □

**Scope and Model Mismatch.** Theorem 1 essentially requires the following hypotheses: a) multiband structure (1), b) finite energy, c) known spectral support $\{\omega_k\}_{k=0}^{K-1}, \Omega$, and d) separation from zero frequency $\min_k |\omega_k| > 2\Omega$. Violations of these assumptions yield model mismatch, impacting the multiband signal recovery. In this paper, we mainly focus on performance analysis under timing jitter and bounded sample perturbations, which is elaborated in "Timing Jitter Analysis".

**Design Rule for $h$.** As described in (9), the DR expansion $||g||_{\mathbf{L}_\infty}/\lambda$ scales exponentially with $h$. However, in practice, having a large $h$ amplifies the noise and degrades the recovery precision and stability (see (58)). To mitigate this effect, an effective solution is to reduce delay $T_d$ and increase the channels $L$, *i.e.* increasing the total sampling rates. Hence, given a certain noise level, there is a trade-off between DR expansion, recovery precision and channel redundancy.

**Aggregate Sampling Condition.** Utilizing `USF-MC` architecture in Fig. 5, the aggregate sampling rate can be computed as, $1/T_\lambda = L/T$, and the deviation to the Landau rate $1/T_{\Omega,K} = K\Omega/\pi$ [5] can be computed as,

$$\gamma_\lambda \overset{\text{def}}{=} \frac{T_{\Omega,K}}{T_\lambda} = \frac{\pi}{\Omega T}\frac{L}{K} \overset{(a)}{>} \frac{\left\lceil \frac{\ln\lambda - \ln\|g\|_{\mathbf{L}_\infty}}{\ln((\Omega + \max_k|\omega_k|)T_d)} \right\rceil}{K} + 1 \tag{27}$$

where (a) follows from the RHS of (22)—$\pi \geqslant \Omega P T_d$ and $T = PT_d$. Consequently, the aggregate

sampling factor $\gamma_\lambda$ asymptotically satisfies,

$$\lim_{T_d \to 0} \gamma_\lambda = 1 + \frac{1}{K}, \quad \forall g \in \mathtt{MB}_\Omega^K(\cdot) \tag{28}$$

which characterizes the theoretical bounds on the aggregate sampling rate of `USF-MC`. Furthermore, (28) implies that, a near Landau-rate signal recovery is feasible when the number of basebands, *i.e.* $K$, is sufficiently large.

**Timing Jitter Analysis.** As `USF-MC` leverages multiple channels for signal capture, a potential issue that may arise in practice is reconstruction stability induced by (i) channel synchronization and (2) timing jitter perturbation. To this end, we evaluate the multiband signal recovery under jitter. Denote by $t_n^l = t_n^l + \Delta t_n^l$ the perturbed multi-channel sampling grid; then we have, $\widetilde{g}_n^l = g(t_n^l) = g_n^l + \eta_n^l$, where $\eta_n^l$ is bounded,

$$|\eta_n^l| = \left| \int_{t_n^l}^{t_n^l} \partial_u g\left(u\right) du \right| \leqslant \left( \Omega + \max_k |\omega_k| \right) T_{\mathsf{max}} \left\| g \right\|_{\mathbf{L}_\infty} \tag{29}$$

where $T_{\mathsf{max}} = \max_{n,l} |\Delta t_n^l|$ represents the maximal time offset of the `USF-MC` sampling architecture. Therefore, the sample deviation induced by timing jitter can be interpreted as additive bounded noise $\eta_n^l$, leading to the following corollary:

**Corollary 1.** *Let $g\left(t\right) = \mathtt{MB}_\Omega^K\left(\underline{\theta}\right)$ and the perturbed `USF-MC` samples be $\widetilde{y}_n^l = \mathscr{M}_\lambda(g\left(t_n^l\right))$. Then, $\Delta^{(h_0)} g_n^l$ can be reconstructed up to an error bounded by $\frac{\lambda}{2}$, provided that*

$$T_{\mathsf{max}} < \frac{\lambda}{4\left(\Omega + \max_k |\omega_k|\right) \left\| g \right\|_{\mathbf{L}_\infty}}, \tag{30}$$

$$T_d \leqslant \frac{1}{\Omega + \max_k |\omega_k|} \left( \frac{\lambda}{2 \left\| g \right\|_{\mathbf{L}_\infty}} \right)^{1/h_0}, \tag{31}$$

*where*

$$h_0 = \left\lfloor \frac{\ln \lambda - \ln \left\| g \right\|_{\mathbf{L}_\infty} - \ln\left(\left(\Omega + \max_k |\omega_k|\right) T_{\mathsf{max}}\right)}{\ln 2} - 1 \right\rfloor. \tag{32}$$

*Proof.* By definition, $\widetilde{y}_n^l = \widetilde{g}_n^l - \widetilde{\varepsilon}_n^l = g_n^l + \eta_n^l - \widetilde{\varepsilon}_n^l$. Computing the $h$-th finite difference across channels leads to,

$$\Delta^{(h)} \widetilde{y}_n^l = \Delta^{(h)} g_n^l - \Delta^{(h)} \widetilde{\varepsilon}_{g,n}^l + \Delta^{(h)} \eta_n^l. \tag{33}$$

From (29), we can deduce that,

$$|\Delta^{(h)} \eta_n^l| \leqslant 2^h \left\| \eta_n^l \right\|_{\ell_\infty}, \quad \forall h \in \mathbb{Z}^+. \tag{34}$$

Hence, the constraint on $T_{\mathsf{max}}$ suggests that,

$$|\Delta^{(h_0)} \eta_n^l| \leqslant 2^{h_0} \left( \Omega + \max_k |\omega_k| \right) T_{\mathsf{max}} \left\| g \right\|_{\mathbf{L}_\infty} \leqslant \frac{\lambda}{2}. \tag{35}$$

Furthermore, with the condition on $T_d$ in (31), we can derive,

$$T_d \leqslant \frac{1}{\Omega + \max_k |\omega_k|} \left( \frac{\lambda}{2 \|g\|_{\mathbf{L}_\infty}} \right)^{1/h_0} \Longrightarrow |\Delta^{(h_0)} g_n^l| \leqslant \frac{\lambda}{2}. \tag{36}$$

Thus, $\Delta^{(h_0)} \widetilde{g}_n^l = \Delta^{(h_0)} g_n^l + \Delta^{(h_0)} \eta_n^l$ is bounded by $\lambda$, and since $\Delta^{(h_0)} \widetilde{\varepsilon}_{g,n}^l \in 2\lambda\mathbb{Z}$, we can write,

$$\mathscr{M}_\lambda(\Delta^{(h_0)} \widetilde{y}_n^l) = \Delta^{(h_0)} g_n^l + \Delta^{(h_0)} \eta_n^l \tag{37}$$

which completes the proof. □

**Remark.** Corollary 1 illustrates the system design flow under hardware imperfection—with certain jitter range, how to configure the system parameters $\{\lambda, T_d\}$? Specifically, given timing jitter characterized by $T_{\mathsf{max}}$, the minimal achievable folding threshold can be determined as

$$\lambda > 4 \left( \Omega + \max_k |\omega_k| \right) T_{\mathsf{max}} \|g\|_{\mathbf{L}_\infty}; \tag{38}$$

next, with the specified DR expansion, the deepest finite difference order $h_0$ can be computed, eventually leading to the feasible range of $T_d$.

With $\Delta^{(h_0)} \widetilde{g}_n^l$ recovered from $\Delta^{(h_0)} \widetilde{y}_n^l$ stated in Corollary 1, in practice (finite acquisition), a straightforward approach of finding $\widetilde{g}$ is to solve the linear system of equations formulated in (23), *i.e.* for every $\omega \in [-\frac{\pi}{PT_d}, \frac{\pi}{PT_d}]$, we can obtain,

$$\begin{aligned} \boldsymbol{\gamma}(\omega) &= \left( \mathbf{A}_{h_0}(\mathcal{S}_\omega) \right)^{-1} \mathbf{b}_{h_0}(\omega), \\ \widehat{\widetilde{\mathbf{g}}}(\omega) = \widehat{\mathbf{g}}(\omega) + \boldsymbol{\gamma}(\omega), \quad & \left[ \mathbf{b}_{h_0}(\omega) \right]_l = \sum_{n \in \mathbb{I}_N} \frac{\Delta^{(h_0)} \eta_n^l}{e^{\jmath\omega(nT + lT_d)}} \end{aligned} \tag{39}$$

where $\mathbf{A}_{h_0}(\mathcal{S}_\omega)$ is a generalized Vandermonde matrix constructed by columns of $\mathbf{A}_{h_0}$ with the index set $\mathcal{S}_\omega$ and

$$\widehat{\mathbf{g}}(\omega) = [\widehat{g}\left(\omega + \frac{-2P_0\pi}{T}\right), \cdots, \widehat{g}\left(\omega + \frac{2P_0\pi}{T}\right)]^\top. \tag{40}$$

Next, we evaluate jitter noise energy, *i.e.*

$$\left\| \Delta^{(h_0)} \eta_n^l \right\|_{\ell_2} = \left( \sum_{n \in \mathbb{I}_N} \left| \Delta^{(h_0)} \eta_n^l \right|^2 \right)^{1/2}, \tag{41}$$

$$\left\| \mathbf{b}_{h_0}(\omega) \right\|_{\ell_2} \leqslant \left( \sum_l \left( \sum_{n \in \mathbb{I}_N} \left| \Delta^{(h_0)} \eta_n^l \right| \right)^2 \right)^{1/2} \leqslant \sqrt{NL} \max_l \left\| \Delta^{(h_0)} \eta_n^l \right\|_{\ell_2}. \tag{42}$$

To this end, we first bound $||\Delta^{(h_0)} \eta_n^l||_{\ell_2}$, by definition,

$$\begin{aligned} \left\| \Delta^{(h_0)} \eta_n^l \right\|_{\ell_2} &= \left\| \Delta^{(h_0-1)} \eta_n^{l+1} - \Delta^{(h_0-1)} \eta_n^l \right\|_{\ell_2} \leqslant \left\| \Delta^{(h_0-1)} \eta_n^{l+1} \right\|_{\ell_2} + \left\| \Delta^{(h_0-1)} \eta_n^l \right\|_{\ell_2} \\ &\leqslant 2 \max_l \left\| \Delta^{(h_0-1)} \eta_n^l \right\|_{\ell_2}. \end{aligned} \tag{43}$$

Hence, by induction, we can write,

$$\left\|\Delta^{(h_0)}\eta_n^l\right\|_{\ell_2} \leqslant 2^{h_0} \max_l \left\|\eta_n^l\right\|_{\ell_2}. \tag{44}$$

Then, to bound $||\eta_n^l||_{\ell_2}$, we use the Taylor expansion of $\eta_n^l$,

$$\eta_n^l = g(t_n^l) - g(t_n^l) = \sum_{k=1}^{\infty} \frac{\partial_t^{(k)} g\left(t_n^l\right)}{k!} \left(\Delta t_n^l\right)^k. \tag{45}$$

Since $g \in \mathtt{MB}_{\Omega}^{K}(\cdot)$, using the Minkowski's inequality [58] gives,

$$\left\|\eta_n^l\right\|_{\ell_2} \leqslant \sum_{k=1}^{\infty} \left\| \frac{\partial_t^{(k)} g\left(t_n^l\right)}{k!} \left(\Delta t_n^l\right)^k \right\|_{\ell_2} \leqslant \sum_{k=1}^{\infty} \frac{(T_{\mathsf{max}})^k}{k!} \left\|\partial_t^{(k)} g\left(t_n^l\right)\right\|_{\ell_2}. \tag{46}$$

From Parseval's theorem, we can derive that,

$$\left\|\partial_t^{(k)} g\left(t_n^l\right)\right\|_{\ell_2}^2 = \frac{1}{2\pi} \int_{-\pi}^{\pi} \left| \left(\frac{\omega}{T}\right)^k \widehat{g}_T(\frac{\omega}{T}) \right|^2 d\omega \tag{47}$$

where

$$\widehat{g}_T(\omega) = \sum_{n\in\mathbb{Z}} g\left(t_n^l\right) e^{-\jmath\omega n T}. \tag{48}$$

From Poisson summation formula and the condition on $\{T, T_d\}$ in Theorem 1 and Corollary 1, $\widehat{g}_T(\omega)$ reduces to,

$$\widehat{g}_T(\omega) = \sum_{p=-P_0}^{P_0} \frac{\widehat{g}\left(\omega + \frac{2p\pi}{T}\right)}{T}, \;\; \omega \in \left[-\frac{\pi}{T_d}, \frac{\pi}{T_d}\right]. \tag{49}$$

As a result, with $g \in \mathcal{B}_{\Omega_K+\Omega}$ and (49), we obtain

$$\begin{aligned} \left\|\partial_t^{(k)} g\left(t_n^l\right)\right\|_{\ell_2}^2 &= \frac{T}{2\pi} \int_{-\frac{\pi}{T}}^{\frac{\pi}{T}} \left|(\omega)^k \widehat{g}_T(\omega)\right|^2 d\omega \\ &\leqslant \frac{\left(\Omega_g\right)^{2k} T}{2\pi} \int_{-\Omega_g}^{\Omega_g} \left|\widehat{g}_T(\omega)\right|^2 d\omega \\ &\overset{(b)}{\leqslant} \frac{\left(\Omega_g\right)^{2k}}{2\pi T} P^2 \left\|\widehat{g}\right\|_{\mathbf{L}_2}^2 = \frac{\left(\Omega_g\right)^{2k}}{T} P^2 \left\|g\right\|_{\mathbf{L}_2}^2 \end{aligned} \tag{50}$$

where $\Omega_g = \max_k |\omega_k| + \Omega$ and (b) follows from the Minkowski's inequality [58]. Hence, (46) simplifies to,

$$\left\|\eta_n^l\right\|_{\ell_2} \leqslant \frac{P\left\|g\right\|_{\mathbf{L}_2}}{\sqrt{T}} \sum_{k=1}^{\infty} \frac{\left(\Omega_g T_{\mathsf{max}}\right)^k}{k!} = \frac{P\left(e^{\Omega_g T_{\mathsf{max}}} - 1\right)\left\|g\right\|_{\mathbf{L}_2}}{\sqrt{T}} \tag{51}$$

and thereby with (51), $||\mathbf{b}_{h_0}(\omega)||_{\ell_2}$ can be bounded as,

$$\left\|\mathbf{b}_{h_0}(\omega)\right\|_{\ell_2} \leqslant 2^{h_0}\sqrt{\frac{NL}{T}} P\left(e^{\Omega_g T_{\mathsf{max}}} - 1\right)\left\|g\right\|_{\mathbf{L}_2}. \tag{52}$$

Consequently, the reconstruction error can be bounded as,

$$\|\boldsymbol{\gamma}(\omega)\|_{\ell_2} \leqslant \frac{1}{\sigma_{\mathsf{min}}\left(\mathbf{A}_{h_0}(\mathcal{S}_\omega)\right)} \left\|\mathbf{b}_{h_0}(\omega)\right\|_{\ell_2} \tag{53}$$

where $\sigma_{\mathsf{min}}(\cdot)$ is the minimal singular value (see "Perturbations" in [59]). Note that, $\mathbf{A}_{h_0}(\mathcal{S}_\omega) = \mathbf{B}\mathbf{C}_{h_0}(\mathcal{S}_\omega)$ (see (25)). Next, we evaluate $\sigma_{\mathsf{min}}(\mathbf{B})$ to bound $\sigma_{\mathsf{min}}\left(\mathbf{A}_{h_0}(\mathcal{S}_\omega)\right)$ in (53). To this end, we introduce the following definitions:

$$\Delta_\star = \inf_{|\omega| \leqslant \frac{\pi}{T}} \Delta(\mathcal{S}_\omega), \;\; \Delta(\mathcal{S}_\omega) = \min_{\substack{p,q \in \mathcal{S}_\omega \\ p \neq q}} \min_{r \in \mathbb{Z}} \frac{|p - q + rP|}{P}. \tag{54}$$

Here, we assume the minimal sub-band separation, *i.e.* $\Delta_\star > 1/(L - h_0)$. In multiband sensing context, this is a mild assumption as the disjoint sub-bands generally spread over a wide spectrum. Consequently, we can derive that [60],

$$\sigma_{\mathsf{min}}(\mathbf{B}) \geqslant \sqrt{L - h_0 - \frac{1}{\Delta_\star}}. \tag{55}$$

With $|\omega| \leqslant \frac{\pi}{PT_d}$ in (23), we can deduce that,

$$\left|\omega T_d + \frac{2p\pi}{P}\right| \geqslant \frac{\pi}{P} \Longrightarrow \min\left|\mathbf{c}_{h_0}\right| \geqslant 2^{h_0}\left(\sin\frac{\pi}{2P}\right)^{h_0}. \tag{56}$$

Combining the results above, $\sigma_{\mathsf{min}}\left(\mathbf{A}_{h_0}(\mathcal{S}_\omega)\right)$ is bounded by,

$$\sigma_{\mathsf{min}}\left(\mathbf{A}_{h_0}(\mathcal{S}_\omega)\right) \geqslant \min\left|\mathbf{c}_{h_0}\right| \sigma_{\mathsf{min}}(\mathbf{B}) \geqslant 2^{h_0}\left(\sin\frac{\pi}{2P}\right)^{h_0} \sqrt{L - h_0 - \frac{1}{\Delta_\star}}. \tag{57}$$

Therefore, the spectrum reconstruction error can be bounded,

$$\left\|\widetilde{\widehat{\mathbf{g}}}(\omega) - \widehat{\mathbf{g}}(\omega)\right\|_{\ell_2} \leqslant \frac{\sqrt{NL}P\left(e^{\Omega_g T_{\mathsf{max}}} - 1\right)\|g\|_{\mathbf{L}_2}}{\sqrt{T\left(L - h_0 - \frac{1}{\Delta_\star}\right)}\left(\sin\frac{\pi}{2P}\right)^{h_0}}. \tag{58}$$

Though developed for timing jitter case, it suffices to show that the above analysis and recovery machinery are applicable to measurement distortions such as quantization error and noise.

**Perturbation Mitigation.** Note that, with sufficiently small $T_{\mathsf{max}}$ such that $h_0 \leqslant 1$, the signal recovery error varies linearly with $T_{\mathsf{max}}$ since $e^{\Omega_g T_{\mathsf{max}}} - 1 \approx \Omega_g T_{\mathsf{max}}$; as $T_{\mathsf{max}}$ increases, the error bound exhibits an exponential expansion, impacting the multiband recovery. To mitigate this effect, an effective solution is to first recover $\Delta^{(1)}\widetilde{g}_n^l$ from $\Delta^{(h_0)}\widetilde{g}_n^l$ via iterative anti-difference operation and then reconstruct $g$ using a coarse-to-fine strategy. Denoting by $\Delta^{(-1)}(\cdot)$ the anti-difference operator [29], for $l \in [0, L-2]$, we have,

$$\Delta^{(1)} g_n^l = \Delta^{(-h_0+1)}\left(\Delta^{(h_0)} g_n^l\right) - \sum_{i=0}^{h_0-1} a_i l^i, \;\; a_i \in 2\lambda\mathbb{Z}. \tag{59}$$

The finite energy hypothesis ($g \cap \mathbf{L}_2$, see (1)), enables determining the unknown coefficients $\{a_i\}$

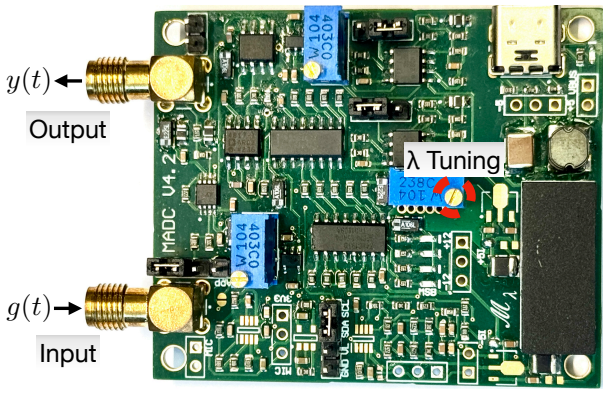


**Fig. 6.** $\mathscr{M}_\lambda$–ADC hardware prototype. The prototype generates a single folded analog output; the multi-channel measurements are emulated by deterministic decimation of the single oversampled sequence with distinct time-delays.

via minimizing the $\ell_2$-norm of the resulting sequence, *i.e.*

$$\{a_i\} = \min_{a_i \in 2\lambda\mathbb{Z}} \sum_{l=0}^{L-2} \left| \Delta^{(-h_0)} \left( \Delta^{(h_0)} g_n^l \right) - \sum_{i=0}^{h_0-1} a_i l^i \right|^2 \tag{60}$$

such that $|\Delta^{(1)} g_n^l| < \infty, l \to \infty$. (60) amounts to a linear system of equations, which can be uniquely solved if $L - 1 \geqslant h_0$. With $\Delta^{(1)} g_n^l$ recovered, we can obtain the rough estimate of $g$ via solving (23) with $h = 1$ and reconstruct the multi-coset samples by definition. By evaluating the deviation between measurements and their reconstruction, the channel-wise DC offset can be retrieved, enabling signal refinement by solving (23) with $h = 0$ (see "Error Mitigation" in Section 3 for details). This method not only suppresses the noise level, but also improves the stability of the multiband recovery operator. Moreover, since (23) is addressed with $h \in \{0, 1\}$, the constraint on the number of channels in Theorem 1 can be relaxed to $L \geqslant \max(h_0, K) + 1$ so that (37) hold.

## 3 Sub-Nyquist Unlimited Sensing in Practice

We have demonstrated a theoretically guaranteed MBS reconstruction (`sNyq`$\lambda$-MB) in Section 2, but the reliance on the hypothesis $c_m \in 2\lambda\mathbb{Z}$ limits robustness in real-world scenarios, potentially compromising HDR and recovery precision. Challenges we have identified via hardware experiments entail:

**Measurement Noise.** System and quantization noise (see (6)) in electronic circuits (see Fig. 6) inevitably give rise bounded-unbounded noise mixture. Amplified noise power destabilizes non-linear filtering (17), degrading signal recovery.

**Hardware Imperfections.** Non-ideal folds may occur in hardware implementation in analog-domain, resulting in off-grid folds or jumps $c_m \notin 2\lambda\mathbb{Z}$. This may induce erratic spikes in (17) and degrade the precision in MBS reconstruction.

This necessitates the development of an empirically robust recovery approach that can tackle noise and folding non-idealities, particularly when operating at sub-Nyquist rate.

**`sNyq`$\lambda$-PMB: Practical Recovery Method.** Here, we leverage sample correlation across channels that were not fully utilized in Theorem 1, which is stated in the result below:

**Lemma 1.** *Let* $g(t) = \mathtt{MB}_{\Omega}^{K}(\underline{\theta})$ *and the shift-difference operator* $\mathcal{S}_{T_d}$ *be defined as* $\mathcal{S}_{T_d}(\cdot) = (\cdot)(t+T_d) - (\cdot)(t)$ *with* $T_d < \frac{1}{\Omega_K+\Omega}$. *Denote by* $\mathsf{H}(t;\mathbf{r}_k) \in P_I$ *the polynomials in* $t$ *with coefficients* $\mathbf{r}_k \in \mathbb{C}^{(I+1)}$ *and degrees no greater than* $I$. *Then,* $g$ *satisfies the approximation property,*

$$\min_{\{\mathbf{r}_k\}_{k\in\mathbb{I}_K}} \max_{t\in[a,b]} \left| \mathcal{S}_{T_d}^{(h)}(g)(t) - \sum_{k=0}^{K-1} \mathsf{H}(t;\mathbf{r}_k)\, e^{\jmath\omega_k t} \right| \leqslant \sigma_{g,h} \tag{61}$$

$$\text{where } \sigma_{g,h} \overset{\text{def}}{=} \frac{(\Omega_K+\Omega)^h T_d^h ((b-a)\Omega)^{(I+1)} \sum_{k=0}^{K-1} \|\varphi_k\|_{\mathbf{L}_\infty}}{2^{(I+1)}(I+1)!}. \tag{62}$$

*Proof.* To prove the lemma, we first show that,

$$\min_{\mathbf{r}_k} \max_{t\in[a,b]} \left|\mathcal{R}_{\varphi_k}(t;\mathbf{r}_k)\right| \leqslant \frac{\|\varphi_k\|_{\mathbf{L}_\infty}\Omega^{(I+1)}(b-a)^{(I+1)}}{2^{(I+1)}(I+1)!} \tag{63}$$

$$\text{where } \mathcal{R}_{\varphi_k}(t;\mathbf{r}_k) \overset{\text{def}}{=} \varphi_k(t) - \sum_{i=0}^{I} r_{k,i}\left(t - \frac{a+b}{2}\right)^i \tag{64}$$

and $\mathbf{r}_k = [r_{k,0},\cdots,r_{k,I}]^\top$. Let

$$\widetilde{r}_{k,i} = \partial_t^{(i)}\varphi_k\left(\frac{a+b}{2}\right)/(i!), \tag{65}$$

then from Taylor's theorem, we have that,

$$\mathcal{R}_{\varphi_k}(t;\widetilde{\mathbf{r}}_k) = \frac{\partial_t^{(I+1)}\varphi_k(\epsilon_I)}{(I+1)!}\left(t-\frac{a+b}{2}\right)^{(I+1)} \tag{66}$$

which is the Lagrange form of the remainder and $\epsilon_I \in [a,b]$. Furthermore, $\mathcal{R}_{\varphi_k}(t;\widetilde{\mathbf{r}}_k)$ is upper bounded by,

$$\max_{t\in[a,b]} \left|\mathcal{R}_{\varphi_k}(t;\widetilde{\mathbf{r}}_k)\right| \overset{(c)}{\leqslant} \frac{\|\varphi_k\|_{\mathbf{L}_\infty}\Omega^{(I+1)}(b-a)^{(I+1)}}{2^{(I+1)}(I+1)!} \tag{67}$$

where (c) follows the Bernstein's inequality [56]. By definition,

$$\min_{\mathbf{r}_k} \max_{t\in[a,b]} \left|\mathcal{R}_{\varphi_k}(t;\mathbf{r}_k)\right| \leqslant \max_{t\in[a,b]} \left|\mathcal{R}_{\varphi_k}(t;\widetilde{\mathbf{r}}_k)\right| \tag{68}$$

which leads to the result shown in (63). Next, let

$$\mathbf{r}_k = \arg\min_{\mathbf{r}'_k} \max_{t\in[a,b]} \left|\mathcal{R}_{\varphi_k}(t;\mathbf{r}'_k)\right|, \quad k\in\mathbb{I}_K \tag{69}$$

then, combining (1), (63) and (69) gives rise to,

$$\left| g(t) - \sum_{k=0}^{K-1} \mathsf{H}(t;\mathbf{r}_k)\, e^{\jmath\omega_k t} \right| \leqslant \frac{((b-a)\Omega)^{(I+1)}}{2^{(I+1)}(I+1)!} \sum_{k=0}^{K-1} \|\varphi_k\|_{\mathbf{L}_\infty} \tag{70}$$

which is obtained by using the triangle inequality. By definition, $\mathcal{S}_{T_d}(g) \in \mathtt{MB}_{\Omega}^{K}(\cdot)$, then plugging $\mathcal{S}_{T_d}(g)$ into the inequality above leads to the result in (61) with $h = 1$. By induction, we can derive the desired result for $h > 1$. □

Lemma 1 provides a *low-dimension representation* of $g(t)$ that belongs to *high-dimension space* $\mathtt{MB}_{\Omega}^{K}(\cdot)$. As a result, the original signal reconstruction can be reformulated as sparse parameter estimation, where the low-dimension parametric approximation acts as an implicit regularizer that restricts the pool of high-dimension solutions to a tightly constrained parameter space, thus enhancing resilience in noisy scenarios [61]. In this paper, we will focus on $h = 1$ (since in noisy scenarios, $h > 1$ can potentially amplify the measurement noise) and use $\underline{y}_n^l = \Delta^{(1)} y_n^l$, $\underline{g}_n^l = \Delta^{(1)} g_n^l$ and $\underline{\varepsilon}_{g,n}^l = \Delta^{(1)} \varepsilon_{g,n}^l$, for notational simplicity. Since, $\underline{g}_n^l = \mathcal{S}_{T_d}(g)(nT + lT_d)$, Lemma 1 provides a *sparse approximation* for $\underline{g}_n^l$ formalized below:

**Proposition 1.** *Let $g(t) = \mathtt{MB}_{\Omega}^{K}(\underline{\theta})$ and $g_n^l = g(nT + lT_d)$, $n \in \mathbb{I}_N, l \in \mathbb{I}_L$ with $T_d < \frac{1}{\Omega_K + \Omega}$. Then, $\{g_n^l\}_{l=0}^{L-1}$ satisfies the following approximation property,*

$$\min_{\{\mathbf{r}_k\}_{k\in\mathbb{I}_K}} \max_{l\in\mathbb{I}_{L-1}} \left| \underline{g}_n^l - \sum_{k=0}^{K-1} \mathsf{H}(l;\mathbf{r}_k)\, e^{\jmath\omega_k T_d l} \right| \leqslant \sigma_g \tag{71}$$

*where*

$$\sigma_g \overset{\text{def}}{=} \frac{(\Omega_K + \Omega)\, T_d((L-1)\Omega T_d)^{(I+1)} \sum_{k=0}^{K-1} \|\varphi_k\|_{\mathbf{L}_\infty}}{2^{(I+1)}(I+1)!}. \tag{72}$$

Proposition 1 can be obtained by plugging $b - a = (L-1)T_d$ into (61). It can be seen that, the approximation error bound $\sigma_g$ in (71) *decays rapidly* as the polynomial degree $I$ increases, especially when $\Omega_K \gg \Omega \Longrightarrow (L-1)\Omega T_d/2 \ll 1$, which naturally holds in multiband spectrum sensing applications [22]. Hence, integrating (71) with (15), the folded samples $\{\underline{y}_n^l\}_{l=0}^{L-2}$ can thus be expressed as,

$$\underline{y}_n^l = \underline{g}_n^l - \underline{\varepsilon}_{g,n}^l, \text{ where } \underline{g}_n^l \approxeq \sum_{k=0}^{K-1} \mathsf{H}(l;\mathbf{r}_k)\, e^{\jmath\omega_k T_d l} \tag{73}$$

$$\underline{\varepsilon}_{g,n}^l = \sum_{m=0}^{M_n-1} c_{n,m}\delta\left[l - z_{n,m}\right], \quad \begin{matrix} c_{n,m} \in 2\lambda\mathbb{Z} \\ z_{n,m} \in \mathbb{I}_{L-1} \end{matrix}. \tag{74}$$

Specifically, $\underline{y}_n^l$ entails two additive components: i) sparse spikes $\underline{\varepsilon}_{g,n}^l$, and ii) modulated low-degree polynomials $\underline{g}_n^l$ with *known* modulation frequency. In real-world scenarios, the signal subspace difference between $\underline{\varepsilon}_{g,n}^l$ and $\underline{g}_n^l$ enables an optimization-based recovery scheme,

formulated as follows:

$$\min_{\substack{\mathbf{c}_n,\mathbf{z}_n\\ \{\mathbf{r}_k\}_{k\in\mathbb{I}_K}}} \left\|\underline{\mathbf{y}}_{w,n} - \underline{\mathbf{g}}_n + \underline{\boldsymbol{\varepsilon}}_{g,n}\right\|_{\ell_2}^2, \text{s.t. } \underline{g}_n^l = \sum_{k=0}^{K-1} \mathsf{H}\left(l;\mathbf{r}_k\right) e^{\jmath\omega_k T_d l} \tag{75}$$

$$\underline{\varepsilon}_{g,n}^l = \sum_{m=0}^{M_n-1} c_{n,m}\delta\left[l - z_{n,m}\right], \quad \begin{matrix} c_{n,m}\in 2\lambda\mathbb{Z} \\ z_{n,m}\in\mathbb{I}_{L-1}\end{matrix} \tag{76}$$

where $\{\underline{\mathbf{y}}_{w,n}, \underline{\mathbf{g}}_n, \underline{\boldsymbol{\varepsilon}}_{g,n}\}$ and $\{\mathbf{c}_n, \mathbf{z}_n\}$ are the vector forms of $\{\underline{y}_{w,n}^l, \underline{g}_n^l, \underline{\varepsilon}_{g,n}^l\}$ and $\{c_{n,m}, z_{n,m}\}$, respectively. Reconstructing $\underline{g}_n^l$ via low-dimensional approximation in (71) enhances resilience against noise, as well as MBS recovery precision.

Solving (75) is challenging due to its non-convexity and constraints. We address this using alternating minimization that decomposes the problem into two tractable sub-problems: P1, which retrieves $\{\mathbf{c}_n, \mathbf{z}_n\}$ via sparse approximation (Section 3.1), and P2, which reconstructs $\underline{\mathbf{g}}_n$ by fitting the modulated polynomial model (Section 3.2).

### 3.1 Sub-Problem P1: Solution Strategy

**Overview.** Assuming that $\underline{\mathbf{g}}_n$ is known, it remains to estimate $\underline{\boldsymbol{\varepsilon}}_{g,n}$ by minimizing,

$$\textsf{P1} \qquad \min_{\{\mathbf{c}_n,\mathbf{z}_n\}} \left\|\widetilde{\underline{\boldsymbol{\varepsilon}}}_{g,n} - \underline{\boldsymbol{\varepsilon}}_{g,n}\right\|_{\ell_2}^2, \text{ s.t. } \widetilde{\underline{\boldsymbol{\varepsilon}}}_{g,n} = \underline{\mathbf{g}}_n - \underline{\mathbf{y}}_{w,n} \tag{77}$$

$$\underline{\varepsilon}_{g,n}^l = \sum_{m=0}^{M_n-1} c_{n,m}\delta\left[l - z_{n,m}\right], \quad \begin{matrix} c_{n,m}\in 2\lambda\mathbb{Z} \\ z_{n,m}\in\mathbb{I}_{L-1}\end{matrix} \tag{78}$$

which is a non-convex problem. $\underline{\boldsymbol{\varepsilon}}_{g,n}$ is the vector form of $\underline{\varepsilon}_{g,n}^l$. To find the solution to (77), we leverage the following continuous-time, sparse parametrization [54]:

$$\underline{\varepsilon}_{g,n}^l = \frac{\mathsf{P}_n(\xi_{L-1}^l)}{\mathsf{Q}_n(\xi_{L-1}^l)}, \quad \begin{matrix}\mathsf{P}_n\in P_{M_n-1}, \\ \mathsf{Q}_n\in P_{M_n}\end{matrix}\ \xi_{L-1}^l = e^{\jmath\frac{2l\pi}{L-1}}. \tag{79}$$

The roots of $\mathsf{Q}_n$ uniquely determine the spike locations $\{z_{n,m}\}$ as $\mathsf{Q}_n(u_{n,m}) = 0 \iff u_{n,m} = e^{\jmath 2\pi z_{n,m}/(L-1)}, m\in\mathbb{I}_{M_n}$. One may find the singularity at $l = z_{n,m}$ with $\mathsf{Q}_n(u_{n,m}) = 0$; however, it can be proven that $\lim_{z\to u_{n,m}} \mathsf{P}_n(z)/\mathsf{Q}_n(z) = c_{n,m}$. Hence, the ratio expression in (79) is well-defined for all $l\in[0, L-2]$. (77) can be equivalently re-formulated as,

$$\min_{\mathsf{Q}_n,\mathsf{P}_n} \sum_{l=0}^{L-2}\left|\underline{\varepsilon}_{g,n}^l - \frac{\mathsf{P}_n(\xi_{L-1}^l)}{\mathsf{Q}_n(\xi_{L-1}^l)}\right|^2. \tag{80}$$

The numerator $\mathsf{P}_n$ can be found exactly by solving a linear system of equations, as soon as the denominator $\mathsf{Q}_n$ is known. Hence, (80) can be considered as minimizing on $\mathsf{Q}_n$ alone.

$$\begin{aligned}\mathbb{E}\left[\left|\widetilde{\underline{g}}_n^{l+1} - \widetilde{\underline{g}}_n^l\right|\right] &\overset{(d)}{\leqslant} \sqrt{2\left(\mathbb{E}\left[\max_{l\in\mathbb{I}_{L-2}}\left|\underline{g}_n^{l+1} - \underline{g}_n^l\right|^2\right] + \mathbb{E}\left[(\underline{w}_n^{l+1} - \underline{w}_n^l)^2\right]\right)} \\ &= \sqrt{2\left(\left(\Omega+\Omega_K\right)^4 T_d^4\left\|g\right\|_{\mathbf{L}_\infty}^2 + 6\sigma_w^2\right)}\end{aligned} \tag{81}$$

**Algorithm 1** **sNyq$\lambda$-PMB: Practical Multiband Signal Recovery**

**Input:** Noisy modulo samples $\underline{\mathbf{y}}_{w,n}$; iteration limits $r_{\max}, i_{\max}, j_{\max}$.
**Output:** Recovered multiband signal $\widetilde{g}$.

**for** $r = 1$ to $r_{\max}$ (initializations) **do**
  $\widetilde{\underline{\varepsilon}}_{g,n}^{[0]} \leftarrow \underline{\mathbf{y}}_{w,n}$
  **for** $i = 1$ to $i_{\max}$ **do**
  *Sub-problem* P1*: residue estimation*
    Initialize $\mathbf{q}^{[0]}$
    **for** $j = 1$ to $j_{\max}$ **do**
      Build $\mathbf{Q}^{[j]}, \mathbf{P}^{[j]}$ via (87)
      $\{\mathbf{q}^{[j]}, \mathbf{p}^{[j]}\} \leftarrow$ solve (91)
      $\underline{\varepsilon}_{g,n} \leftarrow \{\mathbf{q}^{[j]}, \mathbf{p}^{[j]}\}$ via (79)
      **if** (81) holds **then**
        **exit** all loops
      **end if**
    **end for**
    $\{\mathbf{q}^{[i]}, \mathbf{p}^{[i]}\} \leftarrow \{\mathbf{q}^{[j]}, \mathbf{p}^{[j]}\}$
    $\underline{\varepsilon}_{g,n}^{[i]} \leftarrow \{\mathbf{q}^{[i]}, \mathbf{p}^{[i]}\}$ via (79)
    **if** (81) holds **then**
      **exit** all loops
    **else**
      Remove outliers via (95)
    **end if**
  *Sub-problem* P2*: signal recovery*
    $\underline{\mathbf{g}}_n^{[i]} \leftarrow$ (92) and (61)
    $\widetilde{g}^{[i]} \leftarrow$ solve (23) with $\underline{\mathbf{g}}_n^{[i]}$, $h = 1$
    $c_n^{[i]}, \{\widetilde{g}_n^l\} \leftarrow$ (97), (98)
    $\widetilde{g}^{[i]} \leftarrow$ solve (23) with $\{\widetilde{g}_n^l\}$, $h = 0$
  **end for**
**end for**

**Iterative Strategy.** It is challenging to solve (80) due to its non-convex structure [62]. Here, we opt for an iterative strategy, *i.e.* we construct a collection of estimates for $\mathsf{Q}_n$ and choose the one that leads to the minimal mean-squared error on the measurements $\underline{\mathbf{y}}_{w,n}$ via (80). More specifically, these estimates $\{\mathsf{Q}_n^{[j]}\}, j \in \mathbb{I}_{j_{\max}}$ are found iteratively by solving the following approximate problem (assuming $\mathsf{Q}_n^{[j-1]} \approx \mathsf{Q}_n$),

$$\begin{Bmatrix} \mathsf{Q}_n^{[j]} \\ \mathsf{P}_n^{[j]} \end{Bmatrix} = \underset{\mathsf{Q}_n, \mathsf{P}_n}{\arg\min} \sum_{l=0}^{L-2} \left| \frac{\underline{\varepsilon}_{g,n} \mathsf{Q}_n(\xi_{L-1}^l) - \mathsf{P}_n(\xi_{L-1}^l)}{\mathsf{Q}_n^{[j-1]}(\xi_{L-1}^l)} \right|^2. \tag{82}$$

Different initializations of $\mathsf{Q}_n^{[j]}$ yield diverse estimates.

With $\{\mathsf{P}_n, \mathsf{Q}_n\}$ known, locations $\mathbf{z}_n$ can be obtained by root finding—$\mathsf{roots}\left(\mathsf{Q}_n\right) \mapsto \mathbf{z}_n$ since $\mathsf{Q}_n\left(u_{n,m}\right) = 0, m \in \mathbb{I}_{M_n}$. Next, the spike amplitudes are computed via the least-squares,

$$\begin{cases} \widetilde{z}_{n,m} = \dfrac{(L-1)\mathsf{Im}\left(\log u_{n,m}\right)}{2\pi}, \\ \widetilde{c}_{n,m} = \dfrac{-(L-1)u_{n,m}^{-1}\mathsf{P}_n\left(u_{n,m}\right)}{\left(1 - u_{n,m}^{-(L-1)}\right)\partial_u \mathsf{Q}_n\left(u\right)|_{u=u_{n,m}}} \end{cases}, \; m \in \mathbb{I}_{M_n}. \tag{83}$$

Given the on-grid constraints in (77), we then have,

$$\begin{cases} z_{n,m} = \left\lfloor \widetilde{z}_{n,m} + 1/2 \right\rfloor, \\ c_{n,m} = 2\lambda \left\lfloor \left(\widetilde{c}_{n,m} + \lambda\right) / (2\lambda) \right\rfloor \end{cases}, \quad m \in \mathbb{I}_{M_n}. \tag{84}$$

Having estimated the spike parameters $\{\mathbf{c}_n, \mathbf{z}_n\}$, the residue samples can be recovered using (75).

**Algorithmic Implementation.** We offer an algorithm for solving (82). The polynomials

$\{\mathsf{P}_n(\xi_{L-1}^l), \mathsf{Q}_n(\xi_{L-1}^l)\}_{l\in\mathbb{I}_{L-1}}$ in (82) can then be algebraically characterized as,

$$\left[\mathsf{P}_n(\xi_{L-1}^l)\right] = \mathbf{V}_{L-1}^{M_n}\mathbf{p} \;\text{ and }\; \left[\mathsf{Q}_n(\xi_{L-1}^l)\right] = \mathbf{V}_{L-1}^{M_n+1}\mathbf{q} \tag{85}$$

where $\{\mathbf{p}, \mathbf{q}\}$ are the polynomial coefficients of $\{\mathsf{P}_n \in P_{M_n-1}, \mathsf{Q}_n \in P_{M_n}\}$. Assuming the estimate $\mathbf{q}^{[j]}$ at iteration-$j$ is known, the minimization at $j+1$ can be expressed as,

$$\{\mathbf{p}^{[j+1]}, \mathbf{q}^{[j+1]}\} = \underset{\mathbf{p},\mathbf{q}}{\arg\min} \left\|\mathbf{Q}^{[j]}\mathbf{q} - \mathbf{P}^{[j]}\mathbf{p}\right\|_{\ell_2}^2 \tag{86}$$

where the matrices $\{\mathbf{Q}^{[j]}, \mathbf{P}^{[j]}\}$ are respectively given by,

$$\mathbf{Q}^{[j]} = \mathbf{D}\mathbf{R}^{[j]}\mathbf{V}_{L-1}^{M_n+1}, \quad \mathbf{P}^{[j]} = \mathbf{R}^{[j]}\mathbf{V}_{L-1}^{M_n} \tag{87}$$

$$\mathbf{D} = \mathscr{D}_K(\underline{\widetilde{\boldsymbol{\varepsilon}}}_{g,n}),\; \mathbf{R}^{[j]} = \left(\mathscr{D}_K\left(\mathbf{V}_{L-1}^{M_n+1}\mathbf{q}^{[j]}\right)\right)^{-1}. \tag{88}$$

Denote by $\overline{z}$ the conjugate of $z \in \mathbb{C}$. In our formulation, the normalization constraint is given by,

$$\frac{1}{2\pi}\int_0^{2\pi} \overline{\mathsf{Q}_n^{[0]}(e^{\jmath u})}\mathsf{Q}_n^{[j+1]}(e^{\jmath u})\, du = \left(\mathbf{q}^{[0]}\right)^{\mathsf{H}}\mathbf{q}^{[j+1]} = 1 \tag{89}$$

(the middle equality is Parseval's identity), which ensures a unique solution to (86), where $\mathsf{Q}_n^{[0]}$ is the initialization seed of the iterative algorithm. Therefore, the quadratic minimization (86) can be posed as,

$$\{\mathbf{p}^{[j+1]}, \mathbf{q}^{[j+1]}\} = \underset{\mathbf{p},\mathbf{q}}{\arg\min} \left\|\mathbf{Q}^{[j]}\mathbf{q} - \mathbf{P}^{[j]}\mathbf{p}\right\|_{\ell_2}^2 \quad \text{subject to} \quad \frac{1}{2\pi}\int_0^{2\pi} \overline{\mathsf{Q}_n^{[0]}(e^{\jmath u})}\mathsf{Q}_n^{[j+1]}(e^{\jmath u})du = 1 \tag{90}$$

which leads to the update on polynomial estimates

$$\begin{bmatrix}\mathbf{q}^{[j+1]} \\ -\mathbf{p}^{[j+1]}\end{bmatrix} = \nu\left(\begin{bmatrix}\mathbf{Q}^{[j]} & \mathbf{P}^{[j]}\end{bmatrix}^{\mathsf{H}}\begin{bmatrix}\mathbf{Q}^{[j]} & \mathbf{P}^{[j]}\end{bmatrix}\right)^{-1}\begin{bmatrix}\mathbf{q}^{[0]} \\ \mathbf{0}\end{bmatrix} \tag{91}$$

where $\nu$ is the Lagrange multiplier enforcing (89) and $\mathbf{q}^{[0]}$ contains the coefficients of the seed $\mathsf{Q}_n^{[0]}$. The vectors and matrices in (91) have dimensions

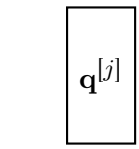


$((M_n+1)\times 1)$

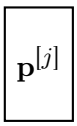


$(M_n \times 1)$




$((L-1)\times(M_n+1))$

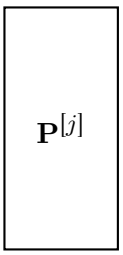


$((L-1)\times M_n)$

### 3.2 Sub-Problem P2: Solution Strategy

**Overview.** With $\underline{\varepsilon}_{g,n}$ known from Section 3.1, finding $\{\mathbf{c}_n, \mathbf{z}_n\}$ boils down to a linearly constrained quadratic minimization problem, which is formulated as,

$$\mathsf{P2} \quad \min_{\{\mathbf{r}_k\}_{k\in\mathbb{I}_K}} \left\| \widetilde{\underline{\mathbf{g}}}_n - \underline{\mathbf{g}}_n \right\|_{\ell_2}^2, \text{ where } \widetilde{\underline{\mathbf{g}}}_n = \underline{\mathbf{y}}_{w,n} + \underline{\varepsilon}_{g,n}, \quad \underline{g}_n^l = \sum_{k=0}^{K-1} \mathsf{H}\left(l; \mathbf{r}_k\right) e^{\jmath\omega_k T_d l}, \ \mathsf{H} \in P_I. \tag{92}$$

**Outlier Elimination.** In the absence of erroneous spikes, the finite difference of $\{\widetilde{\underline{g}}_n^l\}_{l=0}^{L-2}$ in (92) is upper bounded by,

$$\left|\widetilde{\underline{g}}_n^{l+1} - \widetilde{\underline{g}}_n^l\right| \leqslant \left|\underline{g}_n^{l+1} - \underline{g}_n^l\right| + \left|\underline{w}_n^{l+1} - \underline{w}_n^l\right|. \tag{93}$$

From (11), we deduce that,

$$\max_{l\in\mathbb{I}_{L-2}} \left|\underline{g}_n^{l+1} - \underline{g}_n^l\right| \leqslant \left(\Omega + \Omega_K\right)^2 T_d^2 \left\|g\right\|_{\mathbf{L}_\infty} \tag{94}$$

and assuming $w_n^l$ is i.i.d with zero-mean, we have $\mathbb{E}\left[(\underline{w}_n^{l+1} - \underline{w}_n^l)^2\right] = 6\sigma_w^2$, where $\sigma_w = \mathbb{E}\left[w^2\right]$ denotes the noise level[3]. Now, plugging (94) into (93) gives rise to (81), where (d) follows from the QM–AM–GM–HM inequalities. As a result, false spikes in $\widetilde{\underline{\mathbf{g}}}_n$ can be eliminated by thresholding, to impose the smoothness prior on $\widetilde{\underline{\mathbf{g}}}_n$: The signal samples $\widetilde{\underline{g}}_n^l$ with a larger variation than the RHS of (81) are identified as outliers, that is,

$$\mathcal{I}_n = \left\{ l \in \mathbb{I}_{L-1} \;\middle|\; \left|\widetilde{\underline{g}}_n^{l+1} - \widetilde{\underline{g}}_n^l\right| > \epsilon \right\}, \quad \text{where} \quad \epsilon = \sqrt{2\left(\left(\Omega + \Omega_K\right)^4 T_d^4 \left\|g\right\|_{\mathbf{L}_\infty}^2 + 6\sigma_w^2\right)} \tag{95}$$

and are addressed via interpolation techniques, *e.g.* Savitzky-Golay filter [63]. After smoothing $\widetilde{\underline{g}}_n^l$, (92) amounts to a convex problem and can be addressed with an explicit, closed-form solution given by,

$$\underline{\mathbf{g}}_n = \mathbf{H}_g \left(\mathbf{H}_g^{\mathsf{H}} \mathbf{H}_g\right)^{-1} \mathbf{H}_g^{\mathsf{H}} \widetilde{\underline{\mathbf{g}}}_n, \ \ \mathbf{H}_g \in \mathbb{C}^{(L-1)\times(I+1)K} \tag{96}$$

where $\mathbf{H}_g = \left[l^i e^{\jmath\omega_k T_d l}\right]_{l\in\mathbb{I}_{L-1}}^{i\in\mathbb{I}_{I+1}, k\in\mathbb{I}_K}$.

From the optimization standpoint, the recovery problem formulated in (75) can be viewed as sparse decomposition with a concatenated dictionary of polynomial basis and Dirac basis [64]. With a proper choice of $\{T_d, I\}$, it suffices to show that the sparsity of this representation is constrained, suggesting that the underlying sparse decomposition formulated in (75) can be feasibly addressed via $\ell_1$-minimization [64]. In this work, we tackle (75) distinctly through an alternating minimization strategy, which results in an empirically more efficient algorithm due to the polynomial-Dirac space separation.

We initialize $\mathbf{q}^{[0]}$ with i.i.d. Gaussian distribution. The algorithm is restarted if the stopping criterion is not met for $i_{\max}$ initialization seeds. In practice, across extensive numerical and hardware experiment, $\{i_{\max}, j_{\max}, I\} = \{10, 15, 2\}$ is empirically sufficient to find signal estimates satisfying the stopping criterion (81), with an empirical success rate $> 99\%$ over 2 million Monte-Carlo tests (see Section 4).

**Error Mitigation.** In real-world scenarios, from (58), the spectrum recovery error scales largely

[3]The noise level $\sigma_w$ can be estimated from $\mathscr{M}_\lambda$–ADC (modulo ADC) from experimental calibration [32, 49].

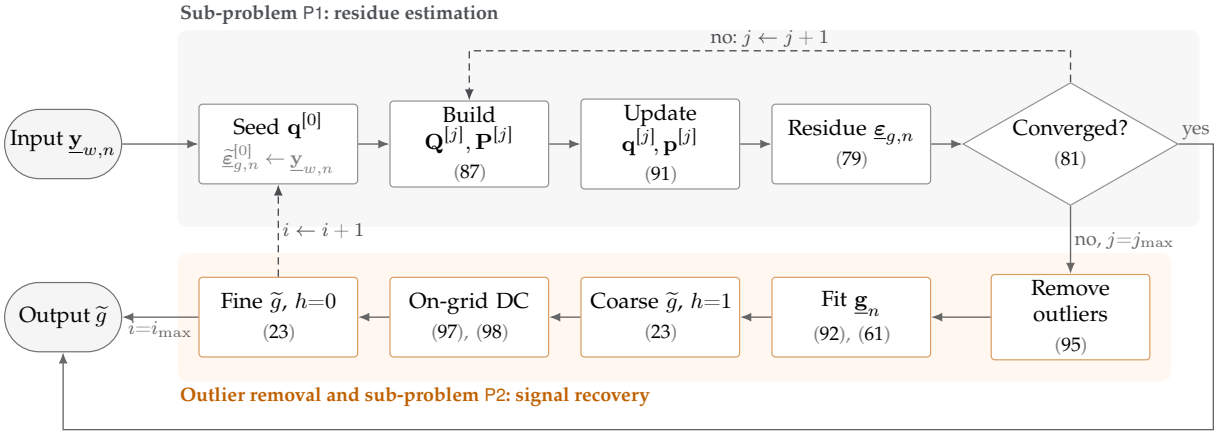


**Fig. 7.** Block diagram of Algorithm 1. Sub-problem P1 (top) estimates the residue $\underline{\varepsilon}_{g,n}$ by iteratively updating the rational-polynomial coefficients $\{\mathbf{q}^{[j]}, \mathbf{p}^{[j]}\}$ (inner loop over $j$). If the consistency test (81) fails after $j_{\max}$ iterations, outliers are removed and sub-problem P2 (bottom) recovers the multiband signal coarse-to-fine, first with $h = 1$ and then with $h = 0$ after on-grid DC estimation; the outer loop over $i$ repeats this, and the whole procedure is restarted from $r_{\max}$ initializations. The algorithm exits as soon as (81) holds.

with $h$, degrading the multiband signal reconstruction quality. To address this problem, we adopt a *practically more robust, multi-stage strategy* leveraging the *measurement consistency. The key insight here is that the multiband structure stated in Theorem 1 allows for signal unfolding of* $\widetilde{g}_n^l$*, enabling reconstruction refinement by tackling the spectrum estimation in* (23) *with* $\mathbf{A}_0$*. Specifically,*

1) Rough reconstruction of $\widetilde{g}$: $\widetilde{g}$ can be reconstructed by solving the linear equations in (23) with $h = 1$.

2) Channel-wise DC estimation: with $\widetilde{g}$, the unknown, on-grid DC offset across channels can be determined as,

$$c_n = 2\lambda \left\lfloor \frac{1}{L} \sum_l \left\lfloor \frac{\widetilde{g}\left(t_n^l\right) - \Delta^{(-1)}\left(\Delta^{(1)} \widetilde{g}_n^l\right)}{2\lambda} + \frac{1}{2} \right\rfloor + \frac{1}{2} \right\rfloor \tag{97}$$

where $\Delta^{(-1)}(\cdot)$ denotes the anti-difference operator, leading to the refinement of $\widetilde{g}_n^l = \Delta^{(0)} \widetilde{g}_n^l$ via

$$\widetilde{g}_n^l = \Delta^{(-1)}\left(\Delta^{(1)} \widetilde{g}_n^l\right) + c_n, \quad n \in \mathbb{I}_N. \tag{98}$$

3) Refinement of $\widetilde{g}$: the signal recovery precision can be enhanced by solving least-squares in (23) with $\{\widetilde{g}_n^l\}$.

The proposed coarse-to-fine approach integrates the on-grid constraint (see (97)) and DC-free multiband signal recovery (see Theorem 1), which operates at $h = 0$ (see (98)) with lower noise floor and improved numerical stability. The procedure of `sNyq`$\lambda$-PMB algorithm is summarized in Algorithm 1, and its data flow is depicted in Fig. 7.

## 4 Experiments

**Overview.** Multiband sensing yields a fundamental trade-off between temporal and amplitude quantization. With the wide spectral support, increasing the sampling rate improves the temporal

redundancy but moves away from the sub-Nyquist objective; enhancing ADC resolution reduces the quantization noise yet does not remove the DR burden before digitization. To address this bottleneck, we adopt a USF-based multi-channel architecture that reduces the sampling rate via structured redundancy while allowing modulo acquisition to manage the amplitude range.

The overarching goal of our experiments is to: 1) validate the results in Theorem 1, 2) comprehensively evaluate the performance of the proposed sNyq$\lambda$-PMB algorithm, and 3) demonstrate the validity of the sNyq$\lambda$-MB approach in real-world lab experiments.

### 4.1 Numerical Experiments

**Overview.** From the acquisition, the multiband signal reconstruction is related to i) input signal DR $\|g\|_{\mathbf{L}_\infty}$, ii) channel redundancy $L$, and iii) quantization bit budget[4] $B$. To this end, we perform comprehensive assessment on the sNyq$\lambda$-MB recovery method supported by Theorem 1 and error mitigation strategy (see "Perturbation Mitigation" in Section 2) across a wide range of $\|g\|_{\mathbf{L}_\infty}$, $L$, and $B$. Note that, the perturbation mitigation strategy relaxes the constraint on $L$ as $L \geqslant \max(h_0, K) + 1$.

**Experimental Protocol.** In order to intuitively evaluate the algorithm performance, we fix $\lambda = 0.10$, $\Omega/(2\pi) = 94.34$ kHz, and $\max_k |\omega_k|/(2\pi) = 4.46$ MHz so that $\|g\|_{\mathbf{L}_\infty}$ and $L$ *directly* characterizes the key acquisition metrics—DR expansion and aggregate sampling factor $\gamma_\lambda$ (see (27)). We first validate Theorem 1 in Section 4.1.1. Then, we assess the multiband signal recovery in the following three setups: i) with a fixed DR $\|g\|_{\mathbf{L}_\infty} = 4\lambda$, we compute the signal reconstruction error with varying bit budget and number of channels (see Section 4.1.2), ii) we maintain the number of channels fixed ($L = 25$) and observe the recovery error with respect to varying bit budget and DR expansion (see Section 4.1.3), and iii) fixing $L = 35$ channels, we evaluate recovery precision under additive white Gaussian noise across varying DR expansions (see Section 4.1.4). With $\lambda$ fixed as a normalization condition, we use the mean-squared error (MSE) in dB ($10\log_{10}$ MSE) to measure the reconstruction accuracy. In each test, we average the MSE over $5000$ realizations with randomized $\underline{\theta} = \{\varphi_k, \omega_k\}_{k\in\mathbb{I}_K}$: 1) the carrier locations are generated from an uniform distribution[5] in the range $(0.19, 4.46]$ MHz, and 2) each baseband waveform is obtained by low-pass filtering different white Gaussian noise realization with cut-off frequency of $\Omega$. The resulting signal realization $g$ is normalized to meet $\|g\|_{\mathbf{L}_\infty} = \mathsf{DRX} \times \lambda$ where DRX is the predefined dynamic range expansion. We benchmark our algorithm with the conventional ADC (CADC)-based approach [10, 11] using the same experimental setup, such as nominal bit budget. Here, for a $B$-bit quantizer, the CADC quantization step scales as $2||g||_{\mathbf{L}_\infty}/(2^B - 1)$, whereas the $\mathscr{M}_\lambda$–ADC yields a quantization step as $2\lambda/(2^B - 1)$, thus enabling a resolution gain governed by $||g||_{\mathbf{L}_\infty}/\lambda$.

#### 4.1.1 Near Landau Rate Recovery

We validate the derived results in Theorem 1 in the first experiment. We set $T = 5.30$ $\mu$s, $T_d = 10$ ns, $K = 10$ and $L = 11$, where the Landau rate and Nyquist rate are thus given by $1.89$ MHz and $9.10$ MHz, respectively. Here, the band locations and baseband waveforms are randomly

[4]Since the quantization error is bounded ($\leqslant 2\lambda/(2^B - 1)$), the recovery machinery in Corollary 1 and the associated numerical analysis still applies.

[5]If the minimum band separation is not satisfied, *i.e.* $\min_{k_1\neq k_2} |\omega_{k_1} - \omega_{k_2}| < 2\Omega$, then $\{\omega_k\}$ are regenerated with a new random initialization seed.

**Table 2.** Parameters and Performance Metrics for the Numerical and Hardware Experiments

| | Numerical Experiment | | | Hardware Experiment |
|---|---|---|---|---|
| **Figure** | Fig. 8 | Fig. 10 | Fig. 13 | Fig. 14 |
| **Signal** | | | | |
| $\frac{\Omega}{\pi}$ | 188.68 kHz | 188.68 kHz | 188.68 kHz | 27.31 Hz |
| $\frac{\omega_k}{2\pi}$ | $[0.55, 2.26, 3.06, 4.09, 4.46]$ MHz | $[0.29, 0.65, 4.46]$ MHz | $[0.90, 1.60, 2.03, 3.19, 4.46]$ MHz | $[29.13, 82.85, 193.01]$ Hz |
| $\|g\|_{\mathbf{L}_\infty}$ | 0.60 | 0.40 | 0.80 | 1.84 |
| **Acquisition** | | | | |
| $1/T$ | 188.68 kHz | 188.68 kHz | 188.68 kHz | 31.58 Hz |
| $P$ | 530 | 265 | 265 | 37 |
| $L$ | 11 | 25 | 35 | 13 |
| $T_d$ | 10 ns | 20 ns | 20 ns | 856 $\mu$s |
| $\lambda$ | 0.10 | 0.10 | 0.10 | 0.43 |
| $\gamma_\lambda$ | 1.10 | 4.17 | 3.50 | 2.15 |
| **Recovery** | | | | |
| $h$ | 2 | 4 | 5 | 1 |
| **Results** | | | | |
| Bits, USF | — | 10.00 | 7.00 | 6.86 |
| Bits, CADC | — | 10.00 | 7.00 | — |
| MSE, USF | $9.69 \times 10^{-12}$ | $6.11 \times 10^{-7}$ | $3.13 \times 10^{-5}$ | $7.36 \times 10^{-4}$ |
| MSE, CADC | — | $2.23 \times 10^{-5}$ | $3.48 \times 10^{-3}$ | — |

generated. Under this setting, we can derive $\gamma_\lambda = 1.10$, aligning with the result in (28). Detailed experimental parameters are outlined in Table 2.

As illustrated in Fig. 8, our method achieves accurate signal reconstruction up to machine precision, with MSE $= -110.13$ dB. With near Landau rate acquisition, this experiment effectively verifies the theoretical results in Theorem 1 and validates the proposed recovery algorithm.

#### 4.1.2 Evaluation over *B* and *L*

We set $\|g\|_{\mathbf{L}_\infty} = 4\lambda$, $T_d = 20$ ns, $K = 6$ and $T = 5.30$ $\mu$s. Under this setup, both the Landau rate and Nyquist rate are fixed as $1/T_{\Omega,K} = K\Omega/\pi = 1.13$ MHz and $(\max_k |\omega_k| + \Omega)/\pi = 9.10$ MHz, respectively. Next, we evaluate the average reconstruction error over a wide range of bit budget ($B \in [4, 16]$) and number of channels ($L \in [13, 40]$) that leads to an aggregate sampling factor varying from $\gamma_\lambda = 2.17$ ($0.27\times$Nyquist rate) to $\gamma_\lambda = 6.67$ ($0.83\times$Nyquist rate).

The Monte-Carlo test results are illustrated in Fig. 9, leading to the following consequences: 1) Define MSE $\leqslant -30$ dB to be reasonable reconstruction precision. Then, the feasible sampling regime of sNyq$\lambda$-MB method is approximately characterized by $B\gamma_\lambda \geqslant 40$. This empirically outlines the critical sampling condition, for instance, using a 12-bit $\mathscr{M}_\lambda$–ADC, the minimal aggregate sampling factor is thus given by 3.33, 2) Increasing $\gamma_\lambda$ significantly improves the reconstruction precision, which aligns with the bound derived in (58), and 3) The algorithm exhibits distinct performance phases, *e.g.* the blue-grey transition at the top-right region of Fig. 9.

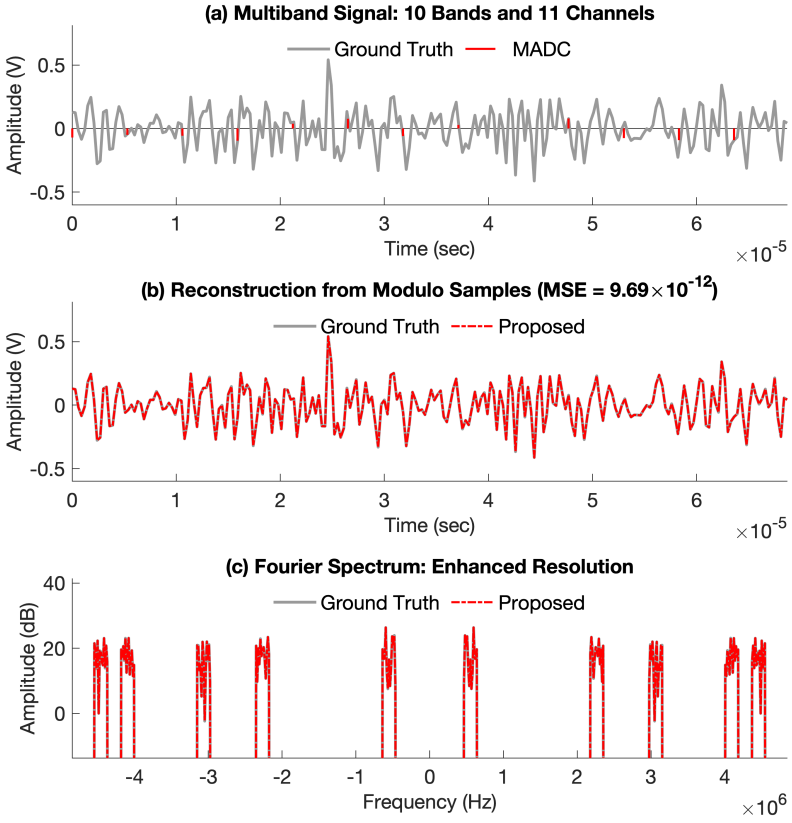


**Fig. 8.** Near Landau rate recovery. With $\gamma_\lambda = 1.10$ and $\|g\|_{\mathbf{L}_\infty} = 6\lambda$, our method attains accurate signal recovery up to machine precision with MSE = –110.13 dB, validating the capability of near Landau rate acquisition.

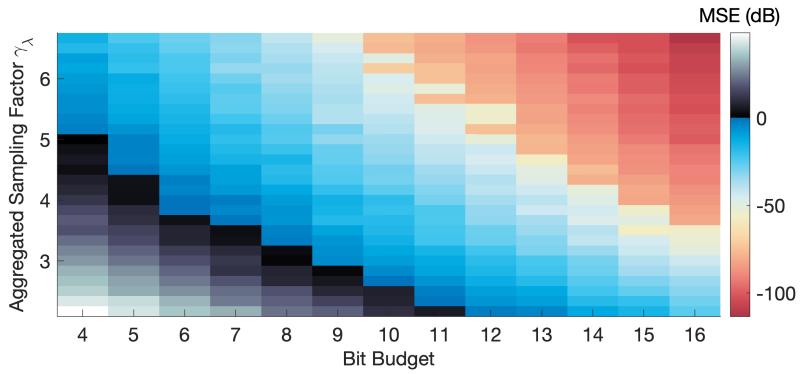


**Fig. 9.** Performance evaluation in terms of $B$ and $\gamma_\lambda$. The reported MSE in each cell is averaged over 5000 realizations with randomized $\underline{\theta} = \{\varphi_k, \omega_k\}$. Empirically, the feasible sampling regime is approximately characterized by $B\gamma_\lambda \geqslant 40$, leading to a reasonable signal recovery with MSE $\leqslant$ –30 dB.

For intuitive evaluation, an example signal recovery is visualized in Fig. 10. The experimental configuration is tabulated in Table 2. Utilizing the identical experimental settings, USF attains a $15.63$ dB accuracy enhancement over the conventional approach, validating the results in Theorem 1.

### 4.1.3 Evaluation over $B$ and $\|g\|_{\mathbf{L}_\infty}$

To compare with the result in Section 4.1.2, we maintain $\{K, \Omega, \max_k |\omega_k|\}$ unchanged, leading to the identical Landau rate and Nyquist rate of $1.13$ MHz and $9.10$ MHz, respectively. To evaluate the recovery precision with regards to the input signal DR, we set $T = 5.30$ $\mu$s, $T_d = 20$ ns, and $L = 25$, giving rise to $\gamma_\lambda = 4.17$ ($0.52\times$Nyquist rate). Then, we assess the average reconstruction MSE over bit budget ($B \in [4, 16]$) and input DR ($\|g\|_{\mathbf{L}_\infty} \in [3, 12]\,\lambda$), as illustrated in Fig. 11.

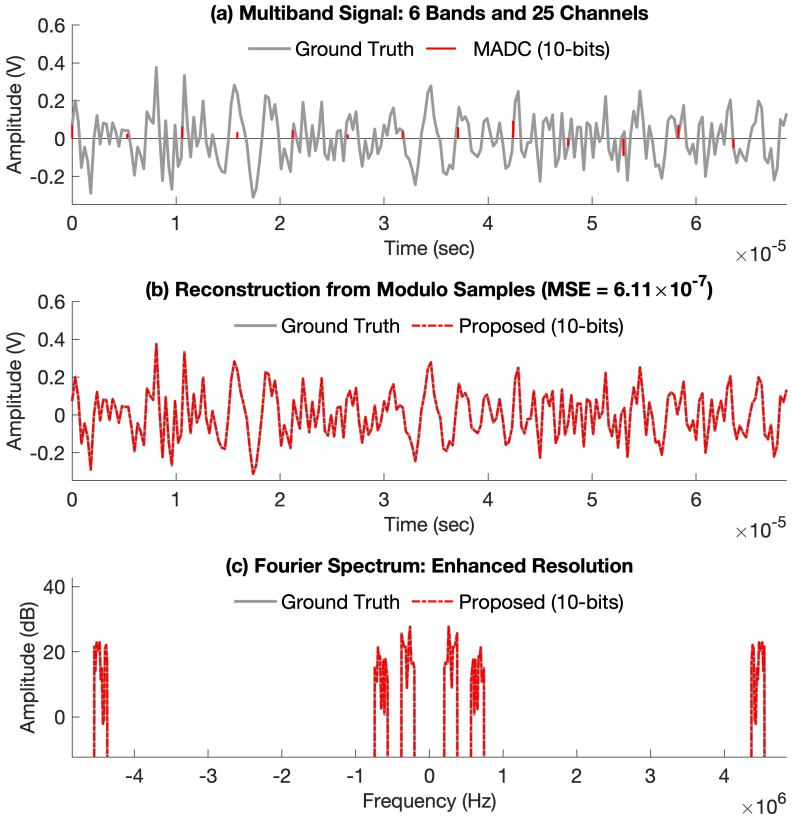


**Fig. 10.** Signal recovery example evaluated in Fig. 9. With $\gamma_\lambda$ = 4.17 and $B$ = 10, the proposed method (MADC) attains an accurate signal reconstruction with MSE = –62.14 dB, demonstrating 15.63 dB improvement over the conventional ADC using the same experimental specifications.

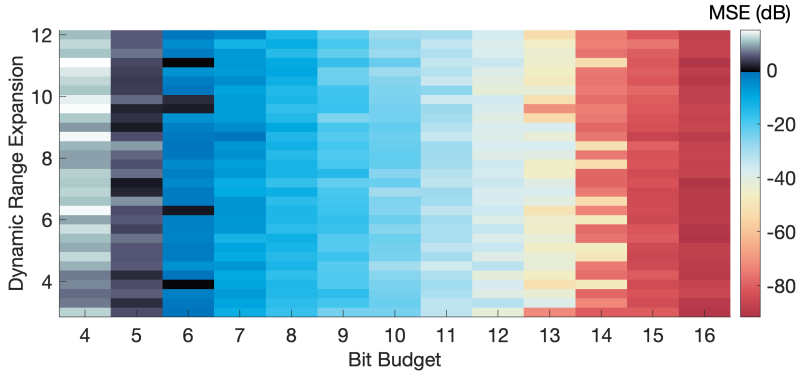


**Fig. 11.** Performance evaluation in terms of $B$ and $\|g\|_{\mathbf{L}_\infty}$. We maintain the acquisition parameters unchanged as Fig. 9 and compute the average MSE over 5000 random realizations. For each bit budget, the algorithm exhibits stable precision across distinct input DR, validating its effectiveness.

From Fig. 11, we can observe that: 1) The feasible sampling regime is approximately the right-half plane of Fig. 11, separated by the line $B = 11$. This is different from the "fan-shaped" feasible area shown in Fig. 9, and 2) With a bit budget larger than the critical value (*e.g.* , 11 bits), the algorithm performance maintains stable across predefined DR.

### 4.1.4 Evaluation over Noise and $\|g\|_{\mathbf{L}_\infty}$

We maintain $\{K, \Omega, \max_k |\omega_k|\}$ unchanged as Section 4.1.3, yielding the Landau rate and Nyquist rate of $1.13$ MHz and $9.10$ MHz, respectively. We use $T = 5.30$ $\mu$s, $T_d = 20$ ns, and $L = 35$, giving rise to $\gamma_\lambda = 5.83$ ($0.73\times$Nyquist rate). The noise $w$ in (6) follows an independent zero-mean Gaussian distribution. We evaluate the algorithm's robustness via the average MSE across distinct SNR

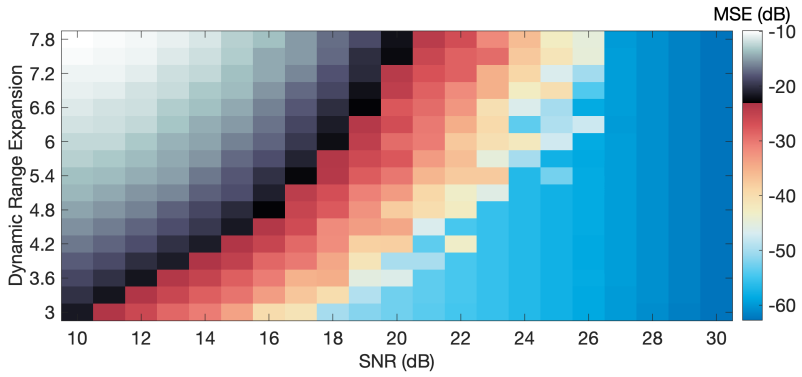


**Fig. 12.** Performance evaluation under additive noise $w$ and $\|g\|_{\mathbf{L}_\infty}$. Using acquisition parameters identical to Fig. 9, we compute the average MSE over 5000 random realizations. The proposed algorithm achieves empirical stable signal recovery across distinct input DRs for SNR $\geqslant$ 24 dB.

([10, 30] dB) and DR expansions ([3, 8] $\lambda$)[6].

As shown in Fig. 12: 1) In low- to moderate-SNR regimes, lower DR expansion improves recovery precision because larger DR expansion generates more *unknown folding parameters*, requiring higher measurement precision., and 2) The proposed method achieves empirically robust performance across varying DR expansions for SNR $\geqslant$ 24 dB.

#### 4.1.5 Weak-Strong Detection

In multiband sensing applications, the mixture of weak and strong targets occurs frequently in practice, *e.g.* , the coexistence of the near-field (NF) and far-field (FF) sources [22, 23]. Due to the distinct propagation distance, the signal power varies largely between NF and FF components. As a result, capturing the mixture of weak and strong components necessitates simultaneous HDR and HDRes sensing capability, particularly in the bit-limited scenarios. To demonstrate this, we conduct the following experiment: we set $T = 5.30$ $\mu$s, $T_d = 20$ ns, $K = 10$, $L = 35$, yielding the Landau rate and Nyquist rate of $1.89$ MHz and $9.10$ MHz with $\gamma_\lambda = 3.50$. The band locations $\{\omega_k\}$ and baseband waveforms $\{\varphi_k\}$ are randomly generated, resulting in $\|g\|_{\mathbf{L}_\infty} = 8\lambda$ and $20$ dB energy contrast between weak and strong components.

The experimental configuration is tabulated in Table 2. Using the same setting ($B = 7$), conventional ADC fails to capture the weak component that is buried beneath the quantization noise floor, as shown in Fig. 13 (c). In contrast, our method achieves a reasonable reconstruction (MSE $= -45.05$ dB), successfully recovering both the strong and weak bands, as shown in Fig. 13 (b) and Fig. 13 (c), respectively.

### 4.2 Folded-Hardware Proof-of-Concept

Beyond numerical experiments, we evaluate the practical multiband signal reconstruction algorithm (Algorithm 1) on folded hardware measurements. As our prototype (Fig. 6) is not intended as an RF-scale realization, the objective here is to validate the proposed recovery algorithm under hardware non-idealities as proof-of-concept.

**Experimental Protocol.** The analog, HDR signal $g$ is fed into the self-designed $\mathscr{M}_\lambda$–ADC (see Fig. 6), which acts as the testbed of our hardware experiments. The prototype generates a single folded analog output; the delayed multi-channel measurements are emulated by deterministic decimation of an oversampled oscilloscope capture. We simultaneously record the original HDR input and $\mathscr{M}_\lambda$–ADC output as ground truth and folded measurements on the PicoScope

[6] SNR is computed with respect to the noiseless modulo samples $\{y_n^l\}$.

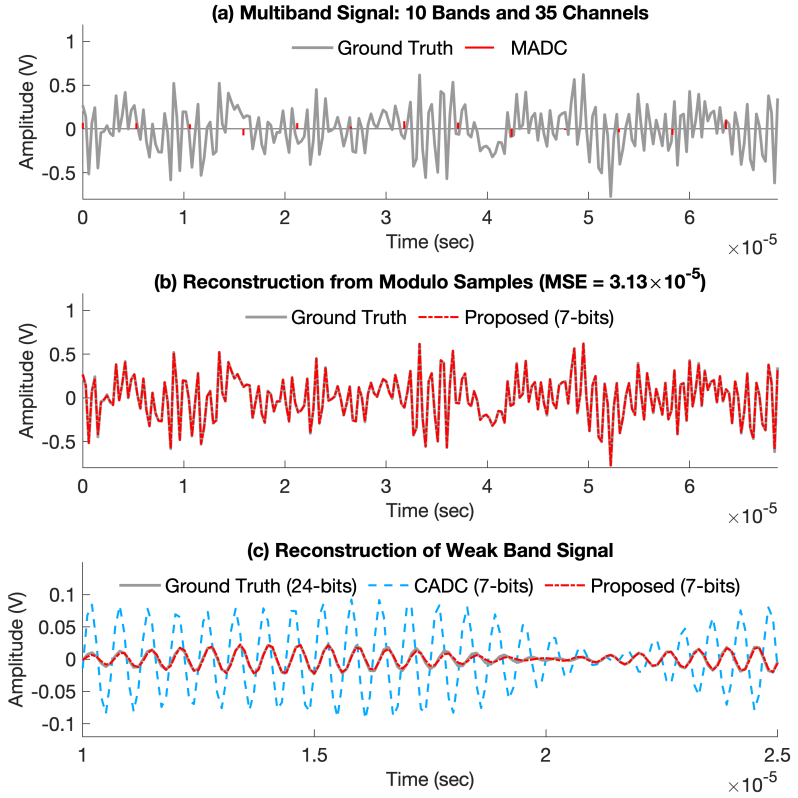


**Fig. 13.** Weak-strong detection. The band locations $\{\omega_k\}$ and baseband waveforms $\{\varphi_k\}$ are randomized, with weak-strong energy contrast up to 20 dB. Utilizing 7 bits, conventional ADC fails to capture the weak component due to the quantization noise; in contrast, the proposed sNyq$\lambda$-MB method precisely retrieves all components with MSE = –45.05 dB.

3406D oscilloscope with $7.62$ bits and $6.86$ bits resolution[7], respectively. We set $T = 31.67$ ms, $T_d = 856$ $\mu$s and $\lambda = 0.43$, leading to $\gamma_\lambda = 2.17$ and $4.27$-fold DR expansion. Other experimental parameters are tabulated in Table 2.

As Algorithm 1 addresses a sparse polynomial-Dirac separation (see (75)), the condition $T_d < \frac{1}{\Omega_K + \Omega}$ is not strictly required, thus relaxing the delay resolution constraint. As shown in Fig. 14, our method attains accurate multiband signal reconstruction with MSE $= -31.33$ dB, demonstrating its effectiveness and advantage in real-world scenarios.

## 5 Conclusions

Sub-Nyquist sampling of multiband signals has been extensively studied as a means to capture high-bandwidth signals where Nyquist-rate sampling is impractical. Yet, most advances have centered on algorithmic design and remain constrained by the fundamental bottleneck of conventional ADCs. In particular, weak–strong band mixtures expose a trade-off between dynamic range and resolution, leading to information loss or coarse quantization. To overcome this, we leverage the Unlimited Sensing Framework (USF), which redefines acquisition through a hardware–algorithm co-design.

The joint use of USF and sub-Nyquist sampling introduces concurrent folding in both amplitude and frequency, complicating recovery under noise and hardware non-idealities.

[7]Each sample is uniformly quantized into $\mathcal{L}$ levels, with bit-depth $\log_2 \mathcal{L}$.

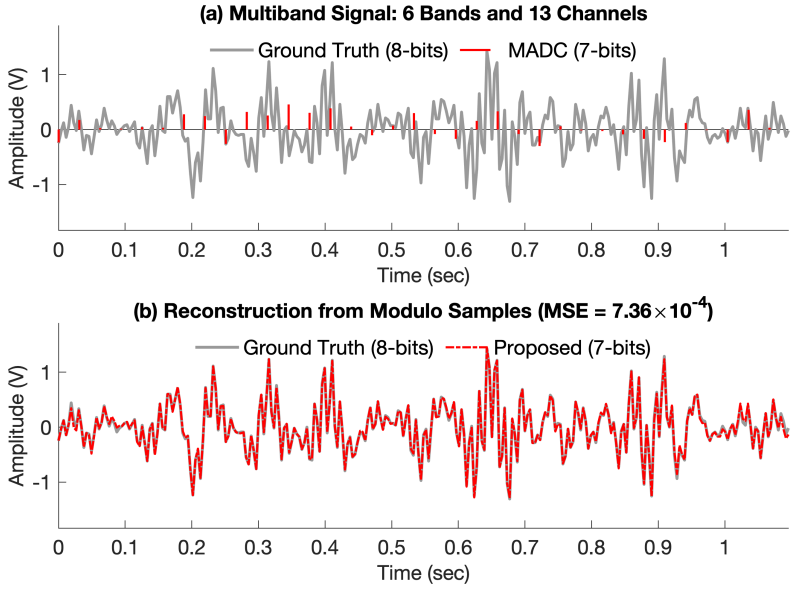


**Fig. 14.** Hardware experiment. Utilizing 2.17× Landau rate and 6.86 bit quantization, the proposed Algorithm 1 yields a precise multiband signal reconstruction with 4.27-fold DR expansion and MSE = –31.33 dB.

We propose a multi-channel sampling architecture, coupled with a sampling theorem and a tailored reconstruction algorithm that can handle measurement distortion and hardware non-idealities. Extensive numerical experiments with hardware validation confirm the performance and advantages of our method. This work lays the groundwork for USF-enabled multiband sensing, paving the way for advances in theory, algorithm design, and practical applications. Future challenges include sharper theoretical guarantees, robust algorithm design, extending to blind multiband sensing, and exploring the integration of USF with hardware platforms.

## References

[1] C. E. Shannon, "A mathematical theory of communication," *Bell System Technical Journal*, vol. 27, no. 3, pp. 379–423, Jul. 1948.

[2] R. Walden, "Analog-to-digital converter survey and analysis," *IEEE J. Sel. Areas Commun.*, vol. 17, no. 4, pp. 539–550, Apr. 1999.

[3] A. Kohlenberg, "Exact interpolation of band-limited functions," *Journal of Applied Physics*, vol. 24, no. 12, pp. 1432–1436, dec 1953.

[4] Y.-P. Lin and P. Vaidyanathan, "Periodically nonuniform sampling of bandpass signals," *IEEE Trans. Circuits Syst. II*, vol. 45, no. 3, pp. 340–351, Mar. 1998.

[5] H. J. Landau, "Necessary density conditions for sampling and interpolation of certain entire functions," *Acta Math.*, vol. 117, no. 0, pp. 37–52, 1967.

[6] P. Feng and Y. Bresler, "Spectrum-blind minimum-rate sampling and reconstruction of multiband signals," in *IEEE Intl. Conf. on Acoustics, Speech and Signal Processing (ICASSP)*, vol. 3, May 1996, pp. 1688–1691.

[7] Y. Bresler and P. Feng, "Spectrum-blind minimum-rate sampling and reconstruction of 2-d multiband signals," in *IEEE Intl. Conf. on Image Processing (ICIP)*, vol. 1, Sep. 1996, pp. 701–704.

[8] R. Venkataramani and Y. Bresler, "Further results on spectrum blind sampling of 2d signals," in *IEEE Intl. Conf. on Acoustics, Speech and Signal Processing (ICASSP)*, vol. 2, Oct. 1998, pp. 752–756.

[9] C. Herley and P. W. Wong, "Minimum rate sampling and reconstruction of signals with arbitrary frequency support," *IEEE Trans. Inf. Theory*, vol. 45, no. 5, pp. 1555–1564, Jul. 1999.

[10] R. Venkataramani and Y. Bresler, "Perfect reconstruction formulas and bounds on aliasing error in sub-Nyquist nonuniform sampling of multiband signals," *IEEE Trans. Inf. Theory*, vol. 46, no. 6, pp. 2173–2183, 2000.

[11] M. Mishali and Y. Eldar, "Blind multiband signal reconstruction: Compressed sensing for analog signals," *IEEE Trans. Sig. Proc.*, vol. 57, no. 3, pp. 993–1009, Mar. 2009.

[12] X.-G. Xia, "On estimation of multiple frequencies in undersampled complex valued waveforms," *IEEE Trans. Sig. Proc.*, vol. 47, no. 12, pp. 3417–3419, Dec. 1999.

[13] L. Xiao and X.-G. Xia, "Frequency determination from truly sub-Nyquist samplers based on robust Chinese remainder theorem," *Signal Process.*, vol. 150, pp. 248–258, Sep. 2018.

[14] P. P. Vaidyanathan and P. Pal, "Sparse sensing with co-prime samplers and arrays," *IEEE Trans. Sig. Proc.*, vol. 59, no. 2, pp. 573–586, Feb. 2011.

[15] S. Qin, Y. D. Zhang, M. G. Amin, and A. M. Zoubir, "Generalized coprime sampling of toeplitz matrices for spectrum estimation," *IEEE Trans. Sig. Proc.*, vol. 65, no. 1, pp. 81–94, Jan. 2017.

[16] N. Fu, Z. Wei, L. Qiao, and Z. Yan, "Short-observation measurement of multiple sinusoids with multichannel sub-Nyquist sampling," *IEEE Trans. Instrum. Meas.*, vol. 69, no. 9, pp. 6853–6869, Sep. 2020.

[17] N. Fu, G. Huang, L. Zheng, and X. Wang, "Sub-Nyquist sampling of multiple sinusoids," *IEEE Signal Process. Lett.*, vol. 25, no. 4, pp. 581–585, Apr. 2018.

[18] J. Mitola and G. Maguire, "Cognitive radio: making software radios more personal," *IEEE Pers. Commun.*, vol. 6, no. 4, pp. 13–18, 1999.

[19] J. Mitola, "The software radio architecture," *IEEE Commun. Mag.*, vol. 33, no. 5, pp. 26–38, May 1995.

[20] M. Mishali and Y. C. Eldar, "From theory to practice: Sub-Nyquist sampling of sparse wideband analog signals," *IEEE J. Sel. Topics Signal Process.*, vol. 4, no. 2, pp. 375–391, Apr. 2010.

[21] M. Mishali and Y. Eldar, "Sub-Nyquist sampling," *IEEE Signal Process. Mag.*, vol. 28, no. 6, pp. 98–124, Nov. 2011.

[22] L. Andrew, "Measurement-based band allocation in multiband CDMA," in *IEEE INFOCOM '99. Conference on Computer Communications.*, 1999, pp. 1364–1371 vol.3.

[23] J. Yang, R. W. Brodersen, and D. Tse, "Addressing the dynamic range problem in cognitive radios," in *IEEE International Conference on Communications*, Jun. 2007, pp. 5183–5188.

[24] V. Venkateswaran and A.-J. van der Veen, "Multichannel $\Sigma\Delta$ ADCs with integrated feedback beamformers to cancel interfering communication signals," *IEEE Trans. Sig. Proc.*, vol. 59, no. 5, pp. 2211–2222, May 2011.

[25] M. Mishali, Y. C. Eldar, O. Dounaevsky, and E. Shoshan, "Xampling: Analog to digital at sub-nyquist rates," *IET circuits, devices & systems*, vol. 5, no. 1, pp. 8–20, 2011.

[26] P. Daponte, L. De Vito, G. Iadarola, M. Iovini, S. Rapuano *et al.*, "Experimental comparison of two mathematical models for analog-to-information converters," in *Proceedings of the 19th IMEKO International Workshop on ADC Modelling and Testing*, 2016, pp. 65–70.

[27] Z. Song, X. Zhang, Z. Chen, R. Tafazolli, and Y. Gao, "Gbsense: A ghz-bandwidth compressed spectrum sensing system," *IEEE Transactions on Circuits and Systems I: Regular Papers*, vol. 72, no. 9, pp. 4912–4924, 2025.

[28] A. Bhandari, F. Krahmer, and R. Raskar, "On unlimited sampling," in *Intl. Conf. on Sampling Theory and Applications (SampTA)*, Jul. 2017.

[29] ——, "On unlimited sampling and reconstruction," *IEEE Trans. Sig. Proc.*, vol. 69, pp. 3827–3839, Dec. 2020.

[30] A. Bhandari, F. Krahmer, and T. Poskitt, "Unlimited sampling from theory to practice: Fourier-Prony recovery and prototype ADC," *IEEE Trans. Sig. Proc.*, pp. 1131–1141, Sep. 2021.

[31] S. Mulleti, E. Reznitskiy, S. Savariego, M. Namer, N. Glazer, and Y. C. Eldar, "A hardware prototype of wideband high-dynamic range analog-to-digital converter," *IET Circuits, Devices & amp; Systems*, vol. 17, no. 4, pp. 181–192, Jun. 2023.

[32] Y. Zhu and A. Bhandari, "Unleashing dynamic range and resolution in unlimited sensing framework via novel hardware," in *2024 IEEE SENSORS*, Oct. 2024, pp. 1–4.

[33] Z. Li, W. Yan, L. Gan, G. Li, and H. Liu, "An FPGA-calibrated modulo ADC for high-dynamic-range signal acquisition," *IEEE Open Journal of Circuits and Systems*, vol. 7, pp. 296–307, 2026.

[34] S. Rudresh, A. Adiga, B. A. Shenoy, and C. S. Seelamantula, "Wavelet-based reconstruction for unlimited sampling," in *IEEE Intl. Conf. on Acoustics, Speech and Sig. Proc. (ICASSP)*, Apr. 2018, pp. 4584–4588.

[35] M. Fanuel and H. Tyagi, "Denoising modulo samples: k-NN regression and tightness of SDP relaxation," *Information and Inference: A Journal of the IMA*, vol. 11, no. 2, pp. 637–677, Oct. 2021.

[36] D. Florescu, F. Krahmer, and A. Bhandari, "The surprising benefits of hysteresis in unlimited sampling: Theory, algorithms and experiments," *IEEE Trans. Sig. Proc.*, vol. 70, pp. 616–630, Jan. 2022.

[37] S. B. Shah, S. Mulleti, and Y. C. Eldar, "Lasso-based fast residual recovery for modulo sampling," in *IEEE Intl. Conf. on Acoustics, Speech and Sig. Proc. (ICASSP)*, Jun. 2023.

[38] N. I. Bernardo, "Short-time Fourier transform-based signal recovery for modulo analog-to-digital converters," *IEEE Access*, vol. 14, pp. 7308–7324, 2026.

[39] Y. Gong, L. Gan, and H. Liu, "Multi-channel modulo samplers constructed from Gaussian integers," *IEEE Signal Processing Letters*, vol. 28, pp. 1828–1832, 2021.

[40] R. Guo and A. Bhandari, "Unlimited sampling of FRI signals independent of sampling rate," in *IEEE Intl. Conf. on Acoustics, Speech and Signal Processing (ICASSP)*, Jun. 2023.

[41] A. Eamaz, K. V. Mishra, F. Yeganegi, and M. Soltanalian, "UNO: Unlimited sampling meets one-bit quantization," *IEEE Trans. Sig. Proc.*, vol. 72, pp. 997–1014, 2024.

[42] N. I. Bernardo, S. B. Shah, and Y. C. Eldar, "Modulo sampling: Performance guarantees in the presence of quantization," *IEEE Trans. Sig. Proc.*, vol. 73, pp. 3829–3842, 2025.

[43] R. Guo, Y. Zhu, and A. Bhandari, "Re-thinking digital audio via unlimited sensing: Theory, algorithms, and hardware validation," *IEEE Trans Audio Speech Lang Process*, pp. 1–16, 2026.

[44] D. Prasanna, C. Sriram, and C. R. Murthy, "On the identifiability of sparse vectors from modulo compressed sensing measurements," *IEEE Signal Process. Lett.*, vol. 28, pp. 131–134, 2021.

[45] G. Joseph, "Noise-resilient unlimited sampling and recovery of sparse signals," in *IEEE Intl. Conf. on Acoustics, Speech and Signal Processing (ICASSP)*, Apr. 2025, pp. 1–5.

[46] Y. Kvich and Y. C. Eldar, "Modulo sampling and recovery in shift-invariant spaces," in *IEEE Intl. Conf. on Acoustics, Speech and Sig. Proc. (ICASSP)*, Apr. 2024, pp. 11–15.

[47] R. Guo and A. Bhandari, "Unlocking off-the-grid sparse recovery with unlimited sensing: Simultaneous super-resolution in time and amplitude," *IEEE J. Sel. Topics Signal Process.*, pp. 1–13, 2025.

[48] G. Shtendel, D. Florescu, and A. Bhandari, "Unlimited sampling of bandpass signals: Computational demodulation via undersampling," *IEEE Trans. Sig. Proc.*, pp. 4134–4145, Sep. 2023.

[49] R. Guo, Y. Zhu, and A. Bhandari, "Sub-Nyquist USF spectral estimation: $K$ frequencies with $6K + 4$ modulo samples," *IEEE Trans. Sig. Proc.*, vol. 72, pp. 5065–5076, 2024.

[50] R. Guo, G. Shtendel, and A. Bhandari, "Multiband unlimited sampling: Super-Nyquist or sub-Nyquist, that is the question!" in *IEEE Intl. Conf. on Acoustics, Speech and Signal Processing (ICASSP)*, Apr. 2025, pp. 1–5.

[51] R. Guo and A. Bhandari, "Spectrum blind unlimited sampling of multi-band signals," in *IEEE Intl. Conf. on Acoustics, Speech and Signal Processing (ICASSP)*, Apr. 2025, pp. 1–5.

[52] G. Shtendel and A. Bhandari, "Unlimited sampling of multiband signals: Single-channel acquisition and recovery," *IEEE Signal Process. Lett.*, pp. 1–5, 2025.

[53] W. P. Zhang and X. Tong, "Noise modeling and analysis of SAR ADCs," *IEEE Trans. VLSI Syst.*, vol. 23, no. 12, pp. 2922–2930, Dec. 2015.

[54] R. Guo and A. Bhandari, "ITER-SIS: Robust unlimited sampling via iterative signal sieving," in *IEEE Intl. Conf. on Acoustics, Speech and Signal Processing (ICASSP)*, Jun. 2023.

[55] J. B. Kruskal, "Three-way arrays: rank and uniqueness of trilinear decompositions, with application to arithmetic complexity and statistics," *Linear Algebra Appl.*, vol. 18, no. 2, pp. 95–138, 1977.

[56] S. M. Nikol'skii, *Approximation of Functions of Several Variables and Imbedding Theorems*. Springer Berlin Heidelberg, 1975.

[57] A. V. Oppenheim, *Signals & systems*. Prentice Hall, 1997.

[58] G. H. Hardy, J. E. Littlewood, and G. Pólya, *Inequalities*. Cambridge University Press, 1952.

[59] G. H. Golub and C. F. V. Loan, *Matrix Computations*. Johns Hopkins University Press, 2013.

[60] C. Aubel and H. Bölcskei, "Vandermonde matrices with nodes in the unit disk and the large sieve," *Appl. Comput. Harmon. Anal.*, vol. 47, no. 1, pp. 53–86, July 2019.

[61] E. J. Candès, J. K. Romberg, and T. Tao, "Stable signal recovery from incomplete and inaccurate measurements," *Comm. Pure Appl. Math.*, vol. 59, no. 8, pp. 1207–1223, Mar. 2006.

[62] K. Steiglitz and L. McBride, "A technique for the identification of linear systems," *IEEE Trans. Autom. Control*, vol. 10, no. 4, pp. 461–464, Oct. 1965.

[63] S. R. Krishnan and C. S. Seelamantula, "On the selection of optimum Savitzky-Golay filters," *IEEE Trans. Sig. Proc.*, vol. 61, no. 2, pp. 380–391, Jan. 2013.

[64] D. L. Donoho and M. Elad, "Optimally sparse representation in general (nonorthogonal) dictionaries via l1 minimization," *Proc. Natl. Acad. Sci.*, vol. 100, no. 5, pp. 2197–2202, 2003.